Received: 25 January 2021 | Revised: 23 August 2021 | Accepted: 29 September 2021 | Published on: 2 November 2021

DOI: 10.1002/qj.4191

Quarterly Journal of the Royal Meteorological Society RMetS

RESEARCH ARTICLE

Dry and moist atmospheric circulation with uniform sea-surface temperature

D. L. Suhas[1,2] | **Jai Sukhatme**[1,3] | **Nili Harnik**[4]

[1]Centre for Atmospheric and Oceanic Sciences, Indian Institute of Science, Bangalore, India

[2]Department of Earth and Planetary Science, University of California, Berkeley, California, USA

[3]Divecha Centre for Climate Change, Indian Institute of Science, Bangalore, India

[4]Department of Geosciences, Tel Aviv University, Tel Aviv, Israel

Correspondence
D.L. Suhas, Centre for Atmospheric and Oceanic Sciences, Indian Institute of Science, Bangalore 560012, India.
Email: suhasdl.mysore@gmail.com

Funding information
University Grants Commission, project F 6-3/2018 under the Indo-Israel Joint Research Program (4th cycle) and Department of Science and Technology, India (DST/CCP/NCM/75/2017) under the Climate Change Programme

Abstract

The steady and transient response of "dynamically" dry and moist atmospheres to uniform sea-surface temperature (SST) is studied using an aquaplanet general circulation model (GCM). Specifically, the latent heat (L_v) of water vapour is varied, so that for small L_v, water substance is essentially a passive tracer from a dynamical point of view. Despite the lack of SST gradients, Hadley and Ferrel cells in the same direction as that on present-day Earth are observed for relatively stronger moist coupling. Organized convergence by equatorial waves drives tropical overturning, and along with the equatorial deformation radius, the Hadley cell width increases with coupling strength. An abrupt switch to a much shallower tropical cell is noted when the system becomes completely passive. Moist static energy is transported equatorward in the tropics and a larger amount is directed poleward in the midlatitudes. As a whole, there is an almost invariant poleward transport of moist static energy for relatively strong coupling of water substance. Transient extratropical activity is seen in the form of intense warm-core vortices for strong coupling, and these systems become weaker and smaller as L_v decreases. The drift of these moist vortices results in the observed poleward energy transport in the midlatitudes. In the tropics, intraseasonal variability is dominant and systematically shifts to longer time periods with stronger coupling. In fact, large-scale, low-frequency Kelvin waves and MJO-like modes disappear as water vapour becomes passive in nature. Further, the direction of tropical overturning reverses as L_v decreases due to the off-equatorial convergence imposed by tropical Rossby waves. Finally, extreme rainfall events associated with cyclonic storms vanish as water vapour becomes dynamically inactive, however, moderate precipitation events increase leading to higher total precipitation for weaker coupling of water substance. Tropospheric heating due to a saturation of the outgoing longwave radiation results in an increase in the stability of the atmosphere for strong coupling, and provides a plausible physical mechanism for interpreting the behaviour of precipitation.

KEYWORDS

Hadley cell, time-dependent flow, uniform surface temperature, water vapour

1 | INTRODUCTION

The explicit response of the atmosphere to uniform lower boundary forcing has proven to be a useful idealization in the climate modelling hierarchy (Maher *et al.*, 2019). Simulations of this kind have yielded insight into possible routes to an organized general circulation (Sumi, 1992; Kirtman and Schneider, 2000; Barsugli *et al.*, 2005; Horinouchi, 2012) and the formation of tropical storm-like vortices and their sensitivity to environmental parameters on an f-plane (Held and Zhao, 2008; Khairoutdinov and Emanuel, 2013; Zhou *et al.*, 2014; Ramírez Reyes and Yang, 2021) as well as on the globe (Shi and Bretherton, 2014; Merlis *et al.*, 2016; Chavas and Reed, 2019) A recent review of these efforts can be found in Merlis and Held (2019). Moist tropical transients, especially the Madden–Julian Oscillation (MJO) have also been studied in uniform sea-surface temperaure (SST) experiments (Grabowski, 2003; Grabowski and Moncrieff, 2004). Further constant-SST experiments have allowed for an examination of convective self-aggregation in a variety of cloud-resolving and parametrized general circulation models (e.g., Wing *et al.*, 2017, 2020). Another motivation comes from paleoclimate estimates that suggest a much weaker meridional gradient in SST during the early Pliocene (Brierley *et al.*, 2009), and it is of interest to understand how such boundary conditions can affect the atmospheric circulation and transient phenomena, especially the frequency and strength of tropical and extratropical cyclones (Fedorov *et al.*, 2010, 2019).

Taking a steady-state view, the large-scale atmospheric circulation and precipitation in aquaplanet models show a strong dependence on the SST profile (Williamson *et al.*, 2013; Oueslati and Bellon, 2013; 2015). In the context of uniform SST, aquaplanet experiments showed the development of an organized tropical atmospheric circulation due to the interaction of moist convection with rotation (Sumi, 1992; Kirtman and Schneider, 2000). This took the form of a well-defined equatorial convergence zone, along with tropical easterlies and subtropical westerlies (Kirtman and Schneider, 2000). Further explorations along these lines showed that the nature of the tropical convergence zone was dependent on the magnitude of the uniform SST. In fact, single, double, symmetric and asymmetric convergence zones were seen to form under differing SST strengths (Barsugli *et al.*, 2005). Interestingly, on varying the threshold relative humidity for triggering the deep moist convection, a uniform SST yielded tropical meridionally overturning cells with vastly differing strengths. In particular, low and high thresholds produced weak and strong moist Hadley cells, respectively (Horinouchi, 2012).

Focusing on transient phenomena, uniform SST runs on an f-plane aimed at understanding rotating radiative–convective equilibrium were seen to result in the spontaneous formation of tropical storm-like vortices (Held and Zhao, 2008). These results were expanded to larger domains (Zhou *et al.*, 2014), and seen to carry over to a spherical geometry where multiple vortices were seen to form, persist and drift poleward (Shi and Bretherton, 2014; Reed and Chavas, 2015). Moreover, the number of systems produced was seen to be dependent on the magnitude of the SST (Khairoutdinov and Emanuel, 2013; Merlis *et al.*, 2016). The genesis of these storms, preferential latitudes and scales of the systems have also been examined in experiments with varying rates of planetary rotation (Chavas and Reed, 2019). In the aforementioned simulations with varying thresholds for triggering deep convection, persistent cyclones along with organized tropical waves were observed in runs with a high relative humidity threshold (Horinouchi, 2012). At long times, after the establishment of zonal mean states, sporadic well-organized eastward propagating convective activity was observed in the Tropics (Sumi, 1992). In fact, detailed simulations with cloud-resolving convective parametrization have noted moisture–convection feedback and the emergence of modes resembling the MJO in flat SST experiments (Grabowski, 2003; Grabowski and Moncrieff, 2004).

From a self-aggregation perspective, uniform SST simulations have demonstrated the spontaneous appearance of organized moist convection and this was attributed to the feedbacks involving cloud–radiative interactions (Bretherton *et al.*, 2005). The sensitivity of aggregation to the resolution of models, the domain size and magnitude of SST have been examined and linked to the differing distribution of clouds in these scenarios (Muller and Held, 2012). Further, the initiation of aggregation and its maintenance were seen to be primarily driven by the short-wave (SW) and long-wave (LW) radiative processes (Wing and Emanuel, 2014). Self-aggregation and its sensitivity to SST has also been observed in general circulation models (Coppin and Bony, 2015; Becker *et al.*, 2017), and this dependence has been examined across various numerical models (Wing *et al.*, 2020). Further, self-aggregation of moisture is believed to play a vital role in the genesis of tropical cyclones and its intensification (Shi and Bretherton, 2014; Muller and Romps, 2018), as well as in the emergence of MJO (Arnold and Randall, 2015).

Here we adopt the viewpoint of treating water vapour as a dynamically active scalar field (Sobel, 2002). In particular, we note that the coupling of water vapour, or any other condensable substance, is controlled by its latent heat (L_v). When $L_v \to 0$, the condensable substance

is advected with the flow, but will not be dynamically coupled to the equations of motion[1]. An interesting question to ask in this uniform SST scenario is, what happens when water vapour is no longer (or only weakly) dynamically active? For example, does the interaction of convection and rotation still result in an organized meridional flow? Do we observe a tropical Hadley cell? Is there a systematic transport of energy across latitudes even without a SST gradient, and if so, why? And how does the partition of latent and dry static energy change in these simulations? What is the nature of the transient tropical wave activity? Specifically, given that the coupling with water vapour is thought to be essential to its existence (Grabowski, 2003; Raymond and Fuchs, 2009; Sobel and Maloney, 2013; Adames and Kim, 2016), do we observe an intraseasonal mode like the MJO when water vapour behaves more like a passive tracer? Further, if there is a change in tropical intraseasonal activity, is it abrupt? How does the nature of the midlatitude synoptic vorticity field change as one progresses from a dynamically dry to a moist atmosphere. Do we always see the formation of tropical storm-like vortices? How about the nature of precipitation and cloud fraction in a world with small L_v?

In all, we believe that these simulations, much like the moist and dry scenarios studied by Frierson *et al.* (2006; 2007), will help in a more robust view of planetary atmospheric circulation regimes in the presence of a condensable substance, especially ones with a different latent heat compared to water vapour. Further, even on present-day Earth, our hope is that exploring the effect of different coupling strengths will help in the understanding of moist geophysical systems – much like the dry and moist simulations of tropical cyclones that are yielding insight into the fundamental nature of these cyclonic systems (Mroweic *et al.*, 2011; Cronin and Chavas, 2019; Wang and Lin, 2020). The modelling framework to address these questions is described in Section 2. The results pertaining to the mean flow and transient activity are presented in Sections 3 and 4, respectively. Section 5 collects and discusses the main findings of our investigation.

2 | MODELLING FRAMEWORK

The aquaplanet experiments are carried out using the Community Atmosphere Model, version 5.3 (CAM 5.3), the atmospheric component of the Community Earth System Model (CESM), version 1.2.2. The model uses a finite-volume dynamical core with a resolution of 0.9° latitude ×1.25° longitude, with 30 vertical levels. Based on the recommendations of Medeiros *et al.* (2016), aerosol effects are minimized by removing the aerosol emissions and by specifying constant droplet and ice number concentrations in the microphysics. The Zhang and McFarlane (1995) convection scheme is used for deep convection, while the University of Washington scheme (UWSC; Bretherton and Park, 2009) is employed for shallow convection. Following Shi and Bretherton (2014), we have used the aquaplanet configuration with a prescribed globally uniform SST of 27 °C. Uniform solar insolation is used with no diurnal cycle (Barsugli *et al.*, 2005; Kirtman and Schneider, 2000) and the solar constant is set to $342\,\mathrm{W\cdot m^{-2}}$. All other fields (like ozone) were set to their annual horizontally averaged values. In essence, except the Coriolis force, no other meridional gradients are present.

To mimic atmospheres with differing strengths of moist coupling, we vary the latent heat of vaporization L_v. Specifically, latent heat is varied everywhere except in the Clausius–Clapeyron equation as detailed in Frierson *et al.* (2006). The degree of moist coupling can also be controlled by varying the amount of moisture in the atmosphere (by varying the saturation vapour pressure at a reference temperature) and keeping L_v fixed (Frierson *et al.*, 2006), but we prefer varying L_v due to the ease in modifying this parameter in the model and the fact that this directly controls the amount of heat released on condensation. Further, changing L_v can potentially be useful in understanding other planetary atmospheres, such as Mars (Read and Lewis, 2004) or Titan (Mitchell and Lora, 2016), which have condensable substances with very different latent heats than water vapour. Specifically, as $L_v \to 0$, water substance is transported by the flow and is active in the radiation budget, but does not lead to latent heating in the dynamical equations of motion. Note that for the $L_v = 0$ run, we also explicitly switch off the evaporation in the model. This is done in order to avoid the numerical issues arising from the $(1/L_v)$ factor in the calculation of evaporative flux. Although we have not explicitly switched off the precipitation, it turns out to be absent for $L_v = 0$, as there are no evaporative sources present. When $L_v > 0$, water substance becomes dynamically active and its strength or coupling with the flow increases with L_v. Perhaps due to excessive amount of heat released, the model fails at latent heats around twice the latent heat of water, so we restrict our experiments to L_v between $1.5X$ and 0, where $X = 2.5 \times 10^6\,\mathrm{J\cdot kg^{-1}}$. The model is run for three years, with the first year of data being discarded as a spin-up time. All results are shown for the last two years of the run.

[1]The so called advection-condensation framework sets $L_v = 0$, and has proven useful in probing the distribution of water vapour in the troposphere and its radiative impacts (O'Gorman and Schneider, 2006; Pierrehumbert *et al.*, 2007; Sukhatme and Young, 2011)

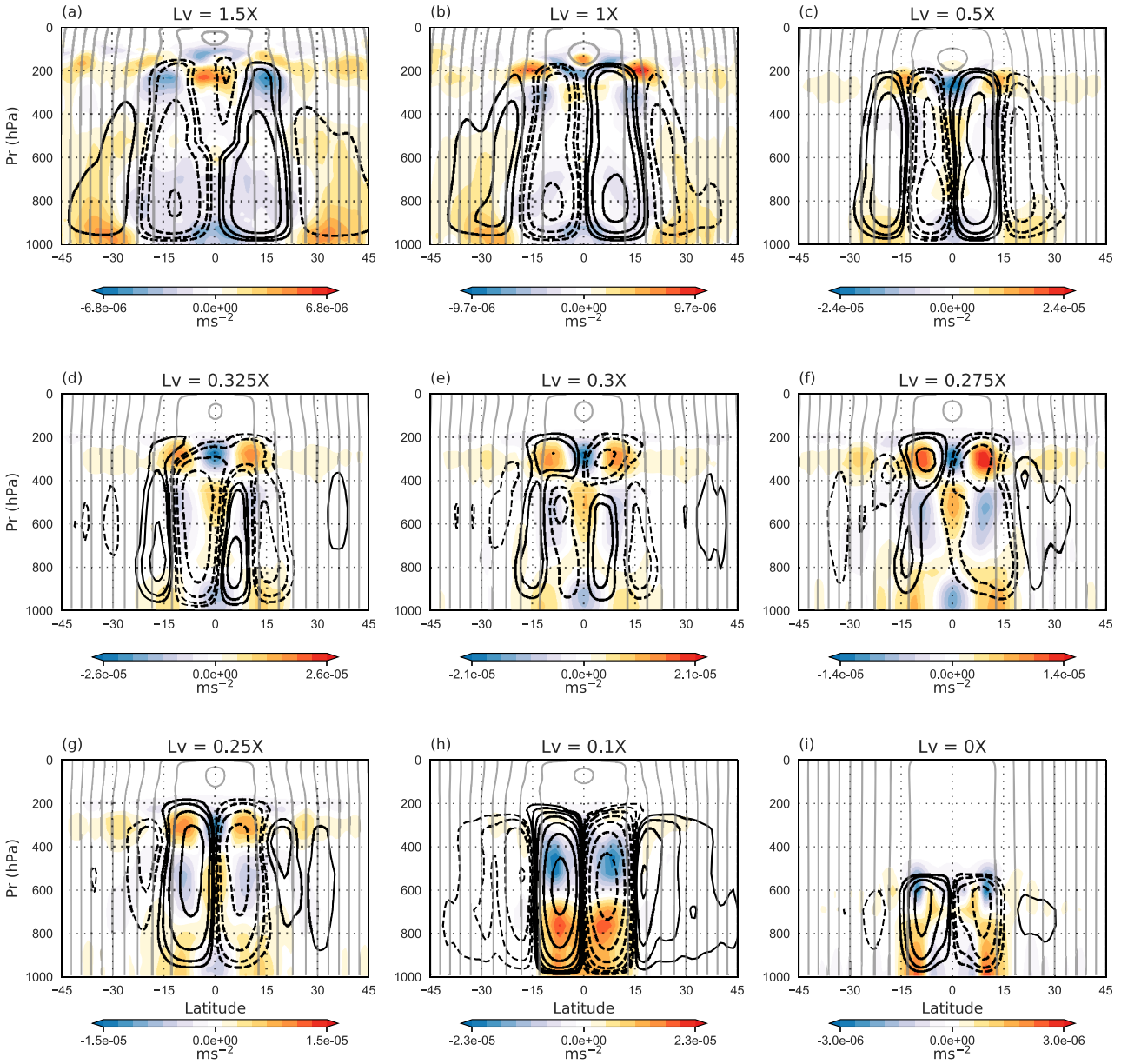

FIGURE 1 Mean meridional mass streamfunction (black contours; solid clockwise and dashed counterclockwise) and angular momentum (grey contours), for nine different values of L_v. The divergence of eddy momentum flux is shown as colour shading. Streamfunction contours are logarithmic in nature, with magnitude doubling between successive contours; the lowest contour has a value of 2.5×10^9 kg·s^{-1} and the zero contour is not shown. Angular momentum contours are at intervals of $0.1\Omega a^2$, with values decreasing away from the Equator [Colour figure can be viewed at wileyonlinelibrary.com]

3 | ZONAL MEAN PICTURE

Even with no solar and surface meridional thermal gradients imposed, a systematic Hadley cell like circulation emerges in all the cases. This is seen in the mean meridional mass streamfunction presented in Figure 1 as a pair of tropical cells straddling the Equator. In addition, weaker oppositely directed Ferrel-like circulation cells are seen in the midlatitudes. For $L_v = 1X$, the meridional streamfunction is of the same order of magnitude, but narrower than that of the annual mean circulation of present-day Earth (Dima and Wallace, 2003; Walker and Schneider, 2005). Usually, the annual mean value is less than the seasonal extremes, but in these simulations there are no seasons and this may explain the comparable magnitude even without a SST gradient. In all these cases, that is, from $L_v = 1.5X$ to 0, the vorticity-based local Rossby number at the extremities of the Hadley cell is between (0.3, 0.6) – thus, idealized theories from limiting cases of Rossby number → 0 or 1 will not immediately be applicable (Walker and Schneider,

2006). The strength of these cells compares well with the results obtained by Horinouchi (2012), although Kirtman and Schneider (2000) obtained much weaker cells with a uniform SST forcing. Further, Horinouchi (2012) observed a weakening of Hadley cell circulation with a lowering of the threshold for moist convection trigger, but we find no significant changes in magnitude with varying L_v. As water vapour becomes passive, the tropical cells become narrower (Figure 1g, h), while the Ferrel cells seem more clearly formed. In fact, there is a systematic decrease in the Hadley cell width from about 25° to 15° as L_v varies from $1.5X$ to 0. Remarkably, for $L_v < 0.3X$, the mean tropical circulation reverses with poleward surface transport in the Tropics. The direction of the mean meridional cells in the midlatitudes also reverses. As seen in Figure 1d, e, f, this transition in the direction of the Hadley Cell takes place around $L_v = 0.3X$. A similar reversal in the atmospheric circulation was observed by Barsugli *et al.* (2005) with variations in insolation and uniform SSTs. As it turns out, the change in direction of the tropical overturning flow is due to the changing nature of dominant waves in the equatorial region; this issue is discussed in Section 4 when transient activity in the system is explored. The limiting case of a dry atmosphere, shown in Figure 1i, indicates a much shallower tropical cell. Comparing Figures 1h and i, the dramatic change in the height of the tropical circulation suggests that the dynamically active nature of moist processes appears to act as a trigger or switch in sustaining the deep convection. In fact, we have performed simulations with $L_v = 0.02X$ and these also show a deep tropical overturning flow, thus supporting the abrupt nature of the transition to a shallow cell when water vapour becomes dynamically passive.

The zonal mean angular momentum contours in Figure 1 are nearly vertical, and flow streamlines cross these contours in each of the runs, indicating a strong influence of eddies in shaping this circulation (Walker and Schneider, 2006; Schneider and Bordoni, 2008). The divergence of the resolved eddy angular momentum flux, $\nabla\cdot\,[\cos\phi\,(\overline{u'v'},\,\overline{u'\omega'})]$, is shown by coloured shading in Figure 1. Unlike eddy fluxes in the present-day atmosphere (Ait-Chaalal and Schneider, 2015), the vertical component of momentum flux convergence is also significant, especially as water vapour becomes passive in nature. Also, these fluxes are dominant in both the upper troposphere and near the surface of the planet. In fact, these flat SST cases constitute an intermediate regime between present-day Earth (where the eddy momentum fluxes are concentrated in the upper troposphere), and reverse surface temperature gradient scenarios on Earth, as well as high-obliquity planets where eddy fluxes are confined near the surface (Ait-Chaalal and Schneider, 2015; Kang *et al.*, 2019). Interestingly, the resolved eddy fluxes seem to account well for the crossing of angular momentum surfaces by the overturning circulation in the lower troposphere, but not so well in the upper troposphere, where their structure is more complex than the overturning circulation. This implies the existence of another momentum sink, possibly unresolved gravity waves which arise near the tropopause, or a numerical sink of momentum (Toniazzo *et al.*, 2020). Further, as L_v becomes smaller, the eddy momentum flux is progressively restricted to the tropical regions.

The zonal mean zonal winds as a function of height and latitude are shown in Figure 2. In all cases, easterlies form through most of the tropical troposphere and a small region of super-rotation is seen directly above the Equator near the tropopause. Indeed, low pole to Equator SST gradients are known to favour tropical super-rotation (Lutsko, 2018). The magnitude of super-rotation becomes weaker, moves into the stratosphere and progressively disappears as $L_v \to 0$. For $L_v \geq 0.5X$ ($L_v = 1.5X, 1X$ and $0.5X$ are shown in Figure 2a–c), westerlies form in the subtropics, though mostly in the lower and middle levels, whereas for lower latent heats, westerlies are pushed equatorward and upwards between 200 and 400 hPa. The momentum flux convergence that is responsible for driving the zonal mean zonal flow is shown in Figure 3. From a flux decomposition (Lee, 1999), we note that transient eddies play a dominant role in the momentum flux budget. This is expected because there is no orography, land–sea contrast or imposed SST structure, hence stationary eddies are absent. Further, the mean meridional circulation also does not have a seasonal cycle and its contribution to the momentum flux convergence is small (Lee, 1999; Dima *et al.*, 2005). As is illustrated for $L_v = 1X$ in Figure 3, the eddy flux convergence drives the upper equatorial super-rotation (Figure 3a), the equatorial easterlies below 200 hPa (Figure 3b) and the westerlies in the midlatitudes from 30–60° below 500 hPa (Figure 3c). Even in other cases, the eddy convergence seems to be primarily responsible for driving the zonal mean flow. In the midlatitudes, we also see a transition from lower-level westerly jets in the Ferrel-like cell regions of the strong moisture coupled runs, to narrow upper-tropospheric and stratospheric westerly jets for the weaker moisture coupled runs. We note that the change from a surface to an upper tropospheric westerly jet goes along with a change in the direction of the overturning cells. In fact, the sharp westerly jets between 200 and 400 hPa at around 15°–20° latitude in the $L_v = 0.1X$ runs are maintained by a vertical advection of zonal momentum via strong ascent at around 600 hPa (Figure 1e). The existence of easterlies at all latitudes for the low moisture coupled runs implies a net gain of atmospheric angular momentum from the surface. This net gain of momentum is actually found in all runs (the globally

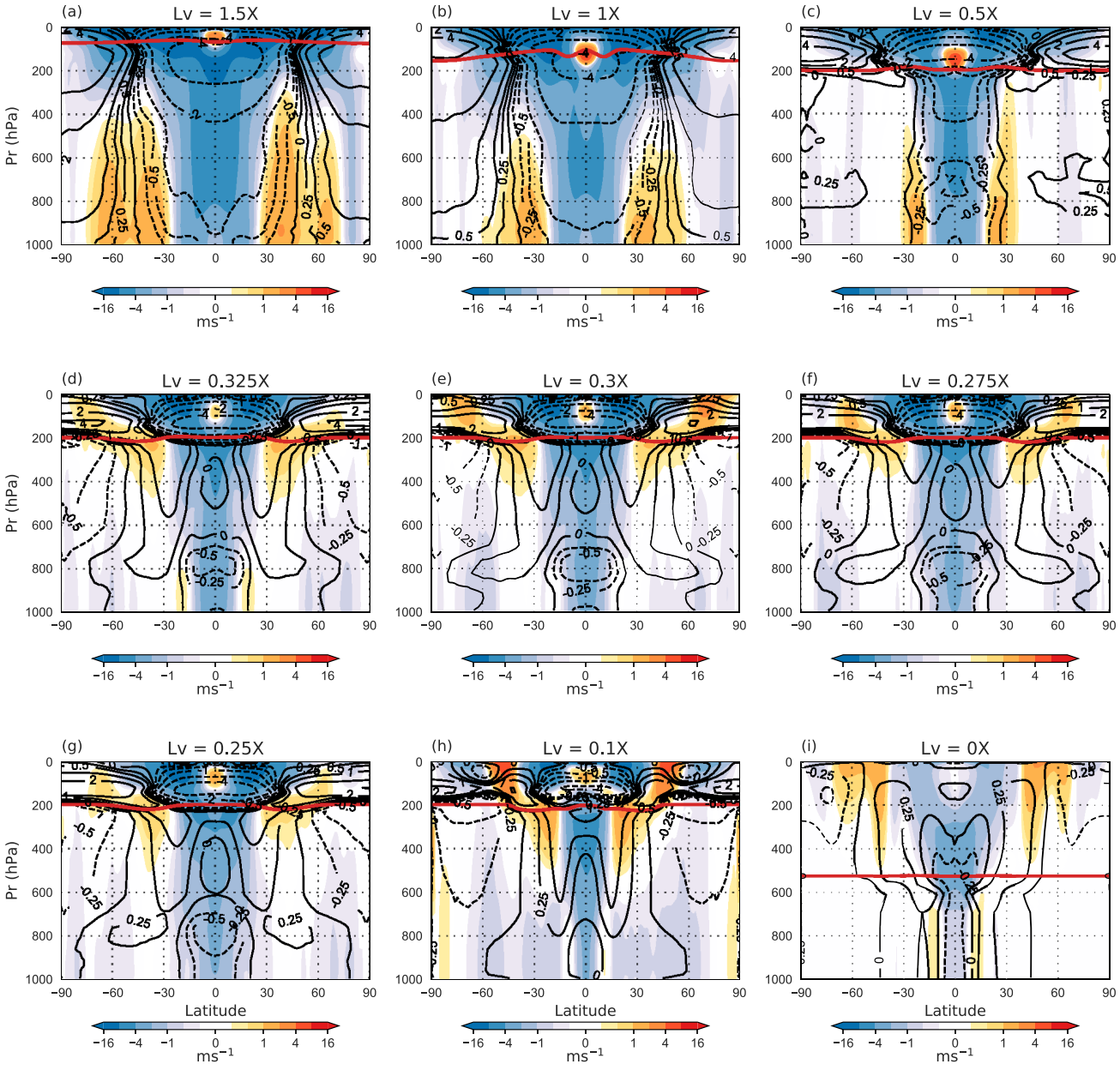

FIGURE 2 As Figure 1, but showing zonal mean zonal wind (colour shading) along with zonal temperature anomalies (black contours). Temperature anomalies are computed by removing the mean at each pressure level; contours are logarithmic in nature with magnitude doubling between successive contours. Tropopause (thick red line) is defined as the level at which the second-order vertical derivative of temperature is a maximum [Colour figure can be viewed at wileyonlinelibrary.com]

averaged surface zonal winds are on average negative for all runs), and is consistent with the model not conserving momentum (Toniazzo *et al.*, 2020).

The zonal mean temperature anomaly, that is, the deviation with respect to the mean on a given pressure level, is also shown in Figure 2. Due to the absence of any prescribed horizontal thermal gradients, the temperature anomalies are much weaker than the typical Earth-like case. While the anomalies are less than 0.5°C in the lower troposphere, the largest anomalies are seen in the upper atmosphere with magnitudes reaching up to 4°C. For $L_v \geq 0.5X$, the Equator is slightly colder than the poles, a feature that was also observed in some of the earlier studies with uniform SSTs (Kirtman and Schneider, 2000; Barsugli *et al.*, 2005; Shi and Bretherton, 2014). Interestingly, for weaker coupling of water vapour, the situation changes and the equatorial region is marginally warmer than the poles. Note that this change in the Equator to pole temperature gradient is accompanied by a reversal in the direction of tropical circulation. Thus, in almost all the cases, the tropical cell is an indirect circulation. In fact, the criterion for a moist direct circulation (Emanuel,

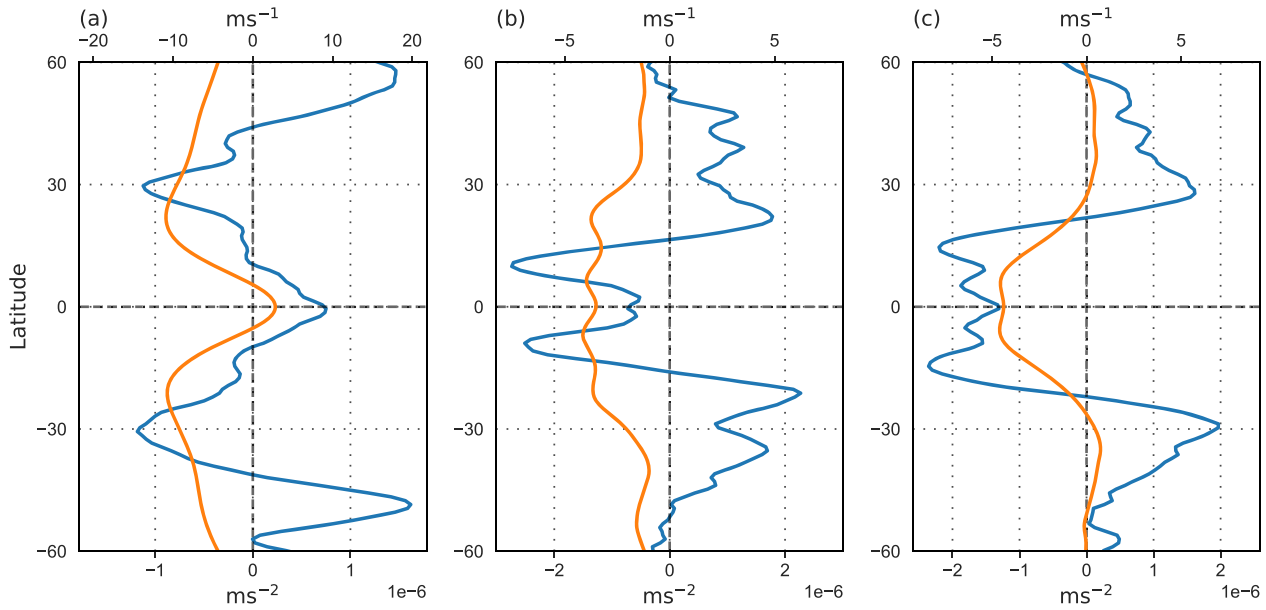

FIGURE 3 Zonal momentum flux convergence (blue, bottom axis) and zonal mean zonal wind (orange, top axis) for $L_v = 1X$. The plots are averaged over (a) 50–150 hPa, (b) 200–400 hPa and (c) 500–800 hPa [Colour figure can be viewed at wileyonlinelibrary.com]

1995) is almost never satisfied by these simulations and, as noted above, the coherent circulation cells in the troposphere are strongly influenced by the eddy fluxes. With a lack of imposed temperature gradients at the surface, the nature of temperature anomalies in the upper troposphere in Figure 2 is consistent with the overturning circulation and its reversal seen in Figure 1. Further, the direction of zonal mean flow in the upper midlatitudes is also in accord with the meridional temperature gradient in the troposphere. We also note that, for $L_v \geq 0.5X$, a poleward increase in lower-tropospheric temperature develops in the midlatitudes. As will be shown later, this gradient develops as a result of poleward drifting warm-core vortices which become more dominant as the moisture coupling increases. For lower L_v values (below $0.5X$), for which warm-core vortices are not dominant, the lower-tropospheric meridional temperature gradients essentially vanish in the midlatitudes, while in the mid-upper troposphere the temperature decreases towards the poles.

Vertical profiles of temperature, potential temperature and equivalent potential temperature are shown in Figure 4. These profiles are colour coded based on different physical and dynamical characteristics, as clarified below. Specifically, the dynamical regime change in Hadley circulation direction is marked by a change from green to orange, as L_v decreases across this transition, while the change in midlatitude meridional temperature gradients from a poleward decrease to increase is marked by the change from blue to green (around $L_v = 0.5X$; Figure 2). Except for the jump between the dry and non-zero L_v runs, where the deepening of the active circulation from 600 hPa to around 200 hPa is evident, the profiles change quite gradually with L_v. The temperature lapse rate increases with decreasing moist coupling, with the $L_v = 0$ approaching the dry lapse rate. Potential temperature increases with height and, in general, lower latent heat cases have lower potential temperature. Equivalent potential temperature is mostly constant up to 200 hPa, especially for the low-coupling case of $L_v = 0.1X$, and to a lesser extent for L_v values around the $0.3X$ transition. For more active cases, equivalent potential temperature decreases till about 700 hPa and then rises gradually up to a height of 200 hPa. As expected, with decreasing moist coupling the equivalent potential temperature and potential temperature profiles converge. The decrease of equivalent potential temperature with height (but not the potential temperature) indicates that the conditions are unstable for moist ascent but stable for dry ascent in the lower troposphere. Further, higher in the troposphere, we note an increase in stability with L_v. This is reminiscent of the present-day Tropics (Holton and Hakim, 2012), but note that here the vertical profiles shown in Figure 4 are similar in the tropical and midlatitudinal regions. Thus, the conditional instability observed for strong coupling is present in the Tropics as well as at higher latitudes. There is a sharp change in potential temperature at upper levels (Figure 4b) roughly coinciding with the level of the tropopause (shown by red line in Figure 2), which bounds the tropical overturning circulation and eddy fluxes. As noted earlier for the dry case, these are confined below 600 hPa.

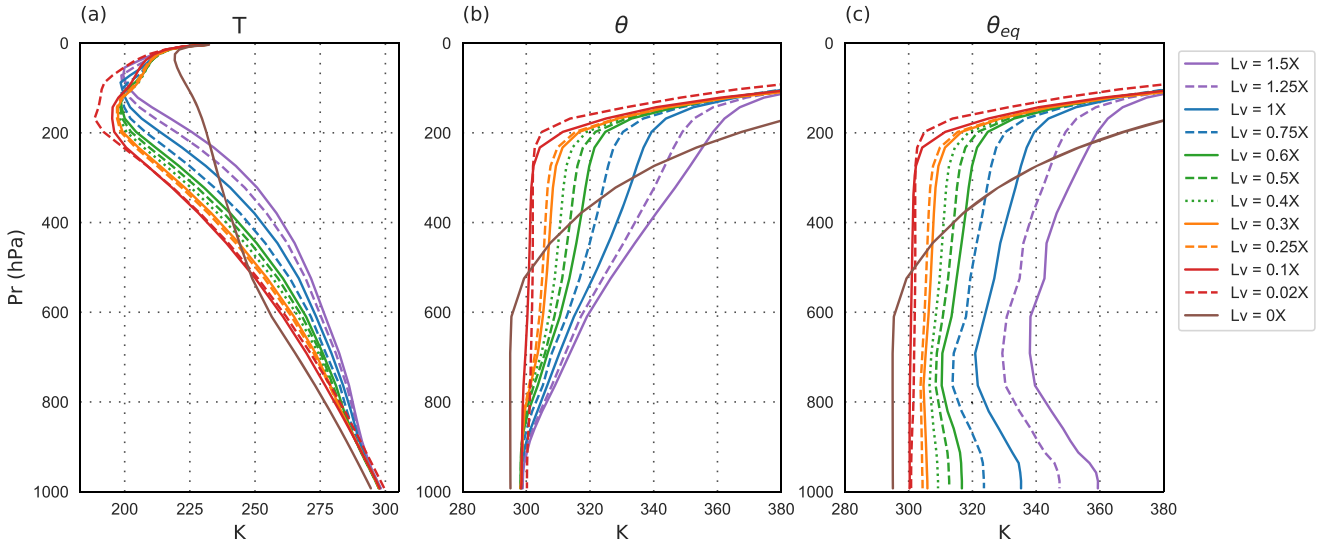

FIGURE 4 Vertical profile of (a) temperature, (b) potential temperature and (c) equivalent potential temperature in the Tropics (within 30°N/S) for different values of L_v. [Colour figure can be viewed at wileyonlinelibrary.com]

The vertically integrated dry and moist static energy fluxes are shown in Figure 5. Moist static energy (MSE), $m = C_pT + gz + L_vq$, comprises the dry static energy $C_pT + gz$ and latent heat energy L_vq. Vertically integrated moist static energy flux is then defined as

$$2\pi a \cos\phi \int_0^{p_s} \frac{\overline{vm}}{g}\, \mathrm{d}P,$$

where ϕ is the latitude, a is the radius of earth, g is the acceleration due to gravity, p_s is the surface pressure and the overbar denotes a time and zonal mean (Frierson *et al.*, 2007). For clarity, we show select cases from the different run-groups (using the same colours as in Figure 4), and plot the two Hadley circulation regimes in two separate rows. Tropical latent heat flux is equatorward (poleward) for higher (lower) latent heats, that is, it mimics the direction of mean circulation at the surface. The dry static energy flux opposes the latent term in the Tropics; thus, MSE transport is determined by the difference of these two opposing components. For the more active cases ($L_v > 0.3X$), the latent term is larger, while for $L_v \leq 0.25X$, the dry static term contributes more to the MSE. But, in all cases, net MSE transport is equatorward in the Tropics and is dominated by the mean flow.

The situation is quite different at higher latitudes. All runs show a poleward latent heat flux, which, as expected, weakens with the moist coupling, and almost vanishes for the weaker coupling runs with equatorial descent ($L_v < 0.3X$). The dry static energy transport has a more complex behaviour. For $L_v > 0.3X$ runs, this flux is equatorward in the subtropics and poleward in midlatitudes. For $L_v < 1X$ (for example, the green curve, Figure 5a) dry fluxes extend all the way to the pole. But, as moist coupling increases, the dry fluxes reduce, resulting in a widening of the subtropical equatorward flux. We note that the Ferrel cells in these runs also expand (Figure 1), suggesting their formation is tied to the equatorward subtropical dry fluxes. As a result, the total poleward flux is quite insensitive to the strength of moist coupling for $L_v \geq 1X$. Such a compensation between changes in latent and sensible heat fluxes, as L_v varies, is reminiscent of a similar compensation found by Frierson *et al.* (2007), when moisture content was varied with a meridional surface temperature gradient. As L_v decreases past the Hadley cell transition ($0.3X$), dry fluxes are poleward everywhere outside the Tropics, and their magnitude decreases as moist coupling reduces. In all, as with the appearance of a coherent tropical overturning circulation, despite the lack of an imposed SST gradient, the atmospheric flow systematically transports energy towards the poles. Though an order smaller than the present-day Earth-like conditions, this transport is robust across the different runs, and is almost invariant for cases with relatively strong moisture coupling.

A decomposition of MSE flux into mean and eddy components (not shown) suggests that the major contribution in the Tropics is from the mean flow, while transient eddies dominate in the midlatitudes. Though, notably, in the subtropics, for the $L_v < 0.3X$ runs, the mean flow due to the Ferrel cell drives potential energy equatorward and dominates the dry, but not the MSE, fluxes. As mentioned before, and will be discussed in detail in Section 4, equatorial waves drive the tropical overturning circulation, which in turn transports MSE meridionally. In the midlatitudes, where eddies directly contribute to the poleward fluxes, it is not *a priori* clear what drives them. For $L_v \leq 0.5X$, we

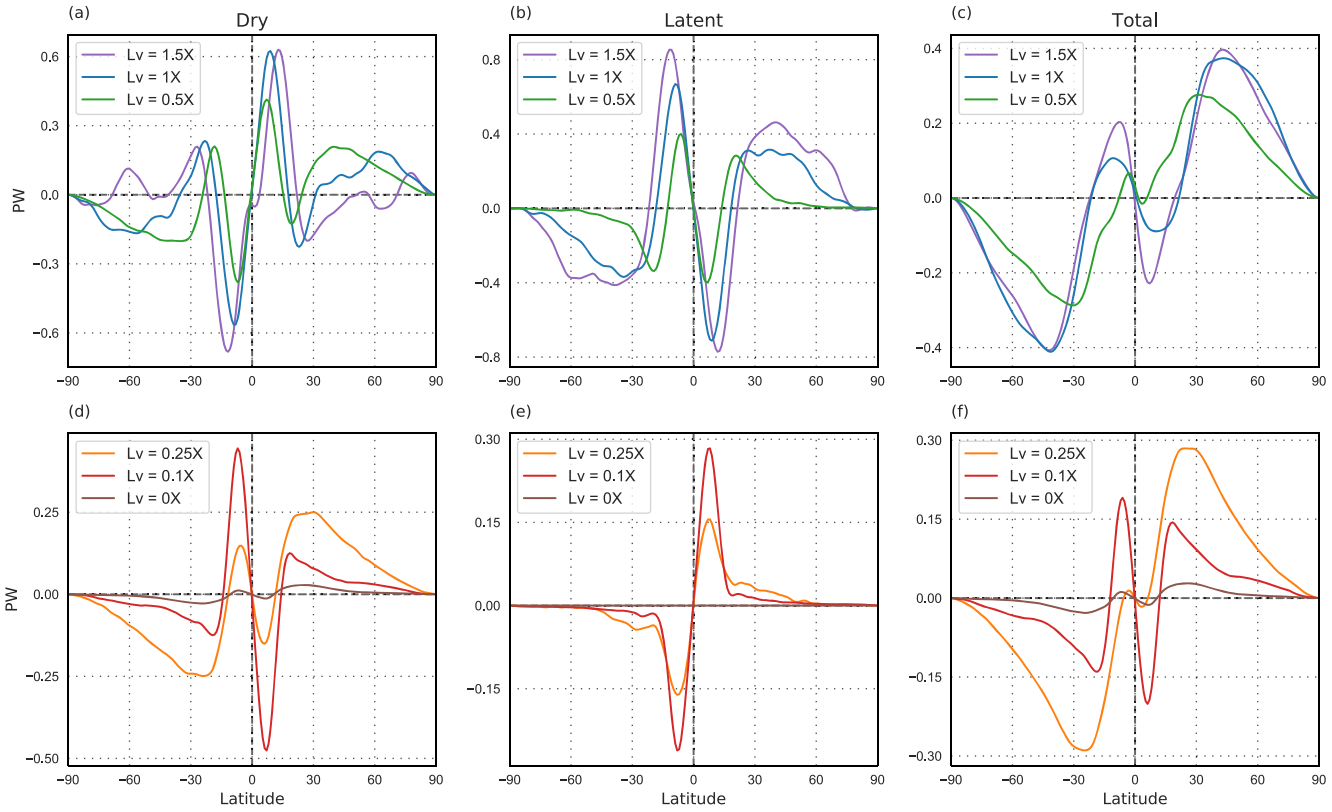

FIGURE 5 Vertically integrated (a, d) dry, (b, e) latent heat and (c, f) moist static energy fluxes for different values of L_v. The same colour coding is used as in Figure 4. (a–c) correspond to a traditionally directed Hadley cell while (d–f) are for a reversed tropical overturning flow [Colour figure can be viewed at wileyonlinelibrary.com]

saw in Figure 2 that the zonal mean temperature decreases poleward in midlatitudes, implying the eddy heat flux is down-gradient and diffusive, leaving us with the question of what gives rise to the temperature gradient in the first place. In the strongly coupled runs ($L_v > 0.5X$), the poles are warmer than lower latitudes, and the eddy heat fluxes are up-gradient. As we will show later on, strong warm-core vortices develop in these runs, which drift poleward, transporting heat and moisture poleward, resulting in the poles warming up.

A net poleward MSE flux implies a net input of energy into the atmosphere at low latitudes, and a net output of energy at high latitudes (Trenberth and Stepaniak, 2003). We examine how the net Energy Input into the Atmosphere (EIA), and its latitudinal gradient, changes with the strength of moisture coupling. Figure 6 shows latitudinal profiles of time and zonal mean net LW radiation fluxes at the surface, latent and sensible heat fluxes, net downward flux of LW radiation at the top of the atmosphere (negative of the outgoing LW radiation; OLR), net atmospheric absorption of SW radiation, and the EIA calculated by summing the above terms. As L_v decreases, surface energy fluxes (top row in Figure 6), all of which act to heat the atmosphere, change from being dominated by latent heat (LH) fluxes, to being dominated by LW radiation. Consistently, the LH fluxes seem to saturate at large L_v (only a small increase between $L_v = 1X$ and $L_v = 1.5X$; Figure 6b), while the surface LW radiation seems to saturate at low L_v values (values similar for $L_v = 0.1X$ and $L_v = 0.25X$ in Figure 6a). We also note opposing latitudinal gradients between LH and LW radiation fluxes, which is due to an opposing dependence on the atmospheric temperature – higher atmospheric temperatures increase LH due to the larger moisture-holding capacity of the air, but they decrease the net upward LW flux at the surface because of the larger downward flux from the atmosphere (while SST is fixed). As a result, the mean latitudinal gradient of these fields changes sign around the transition in meridional temperature gradients which occurs around $L_V = 0.5X$. The sensible heat (SH) fluxes have a relatively small contribution to the overall surface energy budget, however their contribution to the mean latitudinal gradient is significant (Figure 6c), with values being strongest in the Tropics for all runs, but the meridional gradient is largest for large L_v. The other atmospheric heating term is the net SW radiation absorption (Figure 6e). This quantity depends mostly on the clouds, which change in a complex way (especially for small L_v), but its overall contribution peaks at high

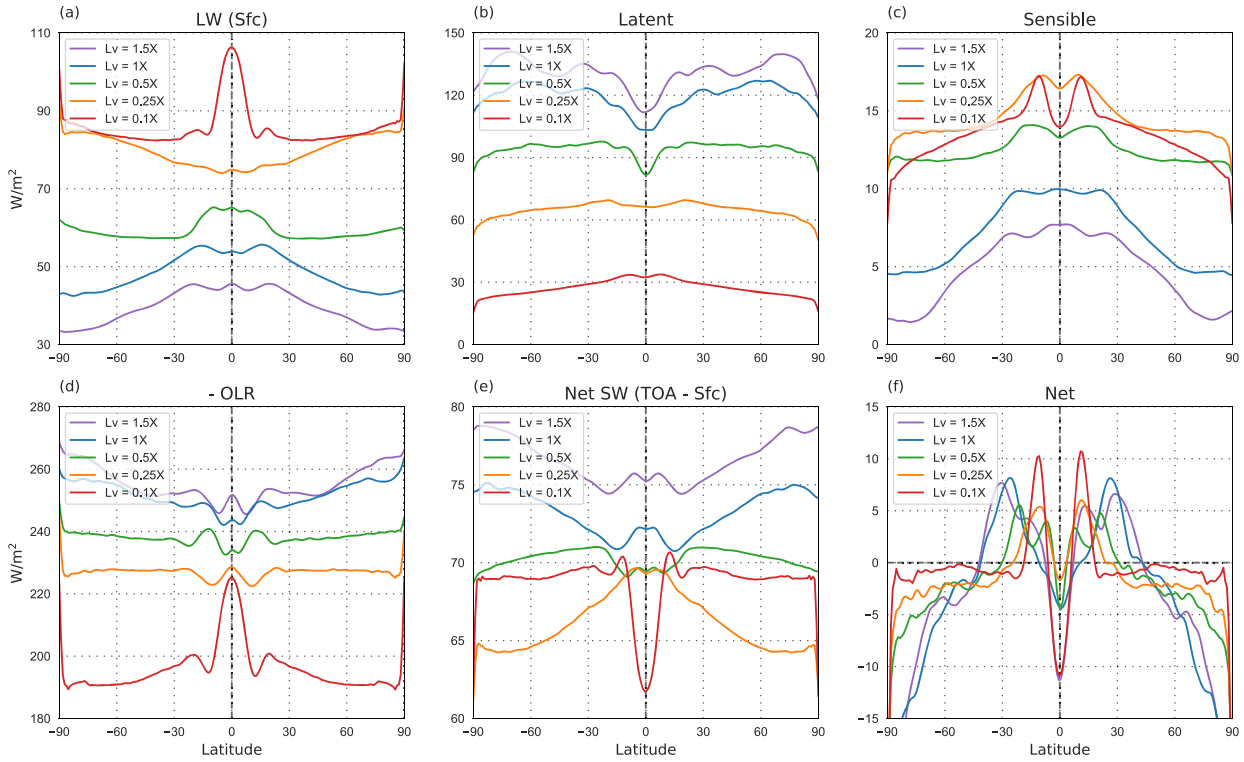

FIGURE 6 Zonal mean time mean fluxes for the simulations with five different values of L_v. The various components are (a) long-wave radiation at the surface, (b) latent heat, (c) sensible heat, (d) downward long-wave radiation at the top (–OLR), (e) net atmospheric absorption of short-wave radiation (top minus surface fluxes), and (f) net flux into the atmosphere. A positive flux implies a net flux into the atmosphere. The colour coding is as used in Figure 4 [Colour figure can be viewed at wileyonlinelibrary.com]

latitudes for large L_v, while for small L_v the latitudinal gradient reverses, and changes strongly especially in the Tropics for $L_v = 0.1X$.

These heating terms are balanced by OLR, which increases with L_v, and saturates at around $L_v = 1X$. The increase in OLR with L_v (up to $L_v = 1X$) is consistent with the decrease in temperature lapse rate as L_v increases, since the LW emitted to space originates in the mid-upper troposphere (Pierrehumbert, 2010). At smallest L_v, OLR has a strong peak in the Tropics, and a flat extratropical profile, but this changes as L_v is increased and the poles become warmer than the Tropics, resulting in peak OLR values at high latitudes for $L_v > 0.5X$. We note that there is a discontinuity at the dry limit, where the atmospheric energy balance changes to a heating by net surface LW flux of around 350 W·m^{-2}, balanced by OLR of about 380 W·m^{-2}, with a small contribution from SW absorption and sensible heat flux, of about 30 W·m^{-2}. Summing all the contributions to get the net EIA (Figure 6f), we see that the atmosphere gains energy in the Subtropics and emits energy in the Extratropics and near the Equator. This is consistent with the subtropical peak of MSE flux for small L_v and the stronger midlatitude peaks of MSE flux for large L_v (Figure 5), and is of course quite different from present-day Earth with differential solar heating. Despite the somewhat noisy latitudinal profile of EIA, we see a clear tendency for the latitudinal gradient to increase with L_v, so that for large L_v, the high latitudes cool most strongly and the Subtropics heat most strongly. This overall increase in the high–low latitude EIA gradient (in absolute value) is consistent with the overall increase in mean poleward MSE flux as L_v increases (Figure 5c, f). It is interesting to again point out that, for strong moisture coupling, the MSE fluxes are upgradient, that is, from the colder Tropics to the warmer poles. Consistently, we will see later that the poleward MSE flux is driven by the dynamics of vortices on a sphere, resulting in the high latitudes being warmer than the Tropics. At small L_v values, the anomalies are more wave-like, and the EIA is dominated by radiative processes (OLR, surface LW flux, and SW absorption) to yield a net positive heating in the Tropics. The wave-like anomalies, in this case, act diffusively and flux MSE poleward, reducing (but not reversing) the temperature gradient.

4 | TRANSIENT DISTURBANCES

In the previous section, we looked at the emergent steady-state zonal mean circulation and its maintenance

by diabatic processes and by eddy MSE and angular momentum fluxes. Given that there is no differential heating imposed in these runs, the underlying processes driving these eddy fluxes are not *a priori* clear. In this section we examine the characteristics of the transient eddies and vortices in more detail. To begin with, the globally integrated kinetic energy (KE) spectra for various scenarios is shown in Figure 7. The KE dominates over available potential energy (Shi and Bretherton, 2014) and, further, the rotational part of the spectrum has much more energy than the divergent component, so Figure 7 is essentially a plot of the rotational kinetic energy. Signs of power-law scaling emerge with stronger moist coupling, and the exponent of the spectrum tends to be around −3 to −4 at intermediate scales and falls off steeply at smaller scales. This exponent is consistent with the known scaling of rotational modes in idealized models of rotating stratified turbulence (e.g., Bartello, 1995; Kitamura and Matsuda, 2006; Sukhatme and Smith, 2008; Vallgren *et al.*, 2011) as well as from midlatitude upper-tropospheric (Nastrom and Gage, 1985; Lindborg, 2015) and ocean surface (Bühler *et al.*, 2014; Rocha *et al.*, 2016; Sukhatme *et al.*, 2020) observations. Further, the scaling persists up to about the deformation scale (Shi and Bretherton, 2014). With weakening moist coupling, the deformation scale reduces with a corresponding shift in the peak of the energy spectra towards the smaller scales (Figure 7). Also, the spectrum becomes "shallower" with decreasing latent heat. In fact, for the passive run, the KE spectrum is more appropriately characterized as a plateau, rather than a power law, with maximum variance near the deformation scale.

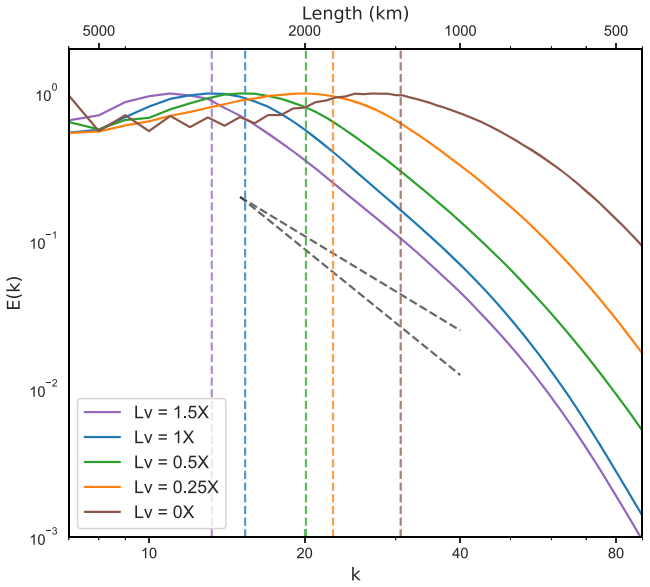

FIGURE 7 Vertically integrated kinetic energy spectra, integrated from the surface to 200 hPa and normalized for easy comparison. Black dashed lines have slopes of −3 and −4. The deformation radius is denoted by the dashed vertical lines. The same colour coding is used as in Figure 4 [Colour figure can be viewed at wileyonlinelibrary.com]

With regard to the Tropics, frequency–wavenumber plots of low-level horizontal winds are shown in Figures 8 and 9. The symmetric and anti-symmetric components are separated and the background spectra are removed. With stronger moist coupling, most of the variability in the symmetric component lies along the linear Kelvin and Rossby wave dispersion curves with Earth-like wave speeds and, much like in other aquaplanet studies (Shi and Bretherton, 2014; Das *et al.*, 2016; Shi *et al.*, 2018), there is an eastward propagating MJO-like signature at low frequencies and large scales. The anti-symmetric part of the spectrum in Figures 8 and 9 shows the presence of mixed Rossby–gravity waves. Further, activity in the 'tropical depression zone' (Wheeler and Kiladis, 1999) is also evident in the stronger coupling runs. It is important to note that these wavenumber–frequency diagrams represent scales larger than those accounted for in the spectra of Figure 7. The intraseasonal modes, especially the eastward moving MJO and Kelvin waves, disappear with decreasing latent heat, that is, as water substance becomes dynamically passive. The lack of an MJO-like mode for weak coupling suggests that this mode of low-frequency activity – at least in this modelling framework – requires interactive moisture (Sobel and Maloney, 2013; Adames and Kim, 2016). The loss of Kelvin waves is evident by the $L_v = 0.25X$ case itself. In fact, together with evidence on the disappearance of Kelvin modes with changes in parameters like the relative humidity threshold for triggering convection (Horinouchi, 2012), convective time-scales (Frierson, 2007) and background saturation fields (Suhas and Sukhatme, 2020), this points to the sensitivity of these waves in the tropical atmosphere. For the limiting case of $L_v = 0$ (Figure 9g,h), it appears that there is not much variability in the Tropics at these large length-scales.

In all simulations, intraseasonal variability (around 20–90 days) is dominant in the Tropics. Specifically, tropical zonal winds in the lower atmosphere are averaged to produce a daily time series whose spectral properties are shown in Figure 10. A sharp distinct peak is observed with stronger coupling, and the dominant period of activity shifts to smaller time-scales with decreasing latent heats (Figure 10a), that is, as $L_v = 1.5X \rightarrow 0.75X$, we note a peak that shifts from about 90 to 30 days. Further, this dominant low-frequency activity is associated with the eastward moving component (Figure 10d). Indeed, these eastward modes (Kelvin and MJO-like systems) are associated with convergence on the Equator and thus drive ascent and result in a "traditional" or present-day Earth-like overturning mean flow (Figure 1). In addition, for $L_v = 1.25X$ and $1.5X$, there is a second window of activity at shorter

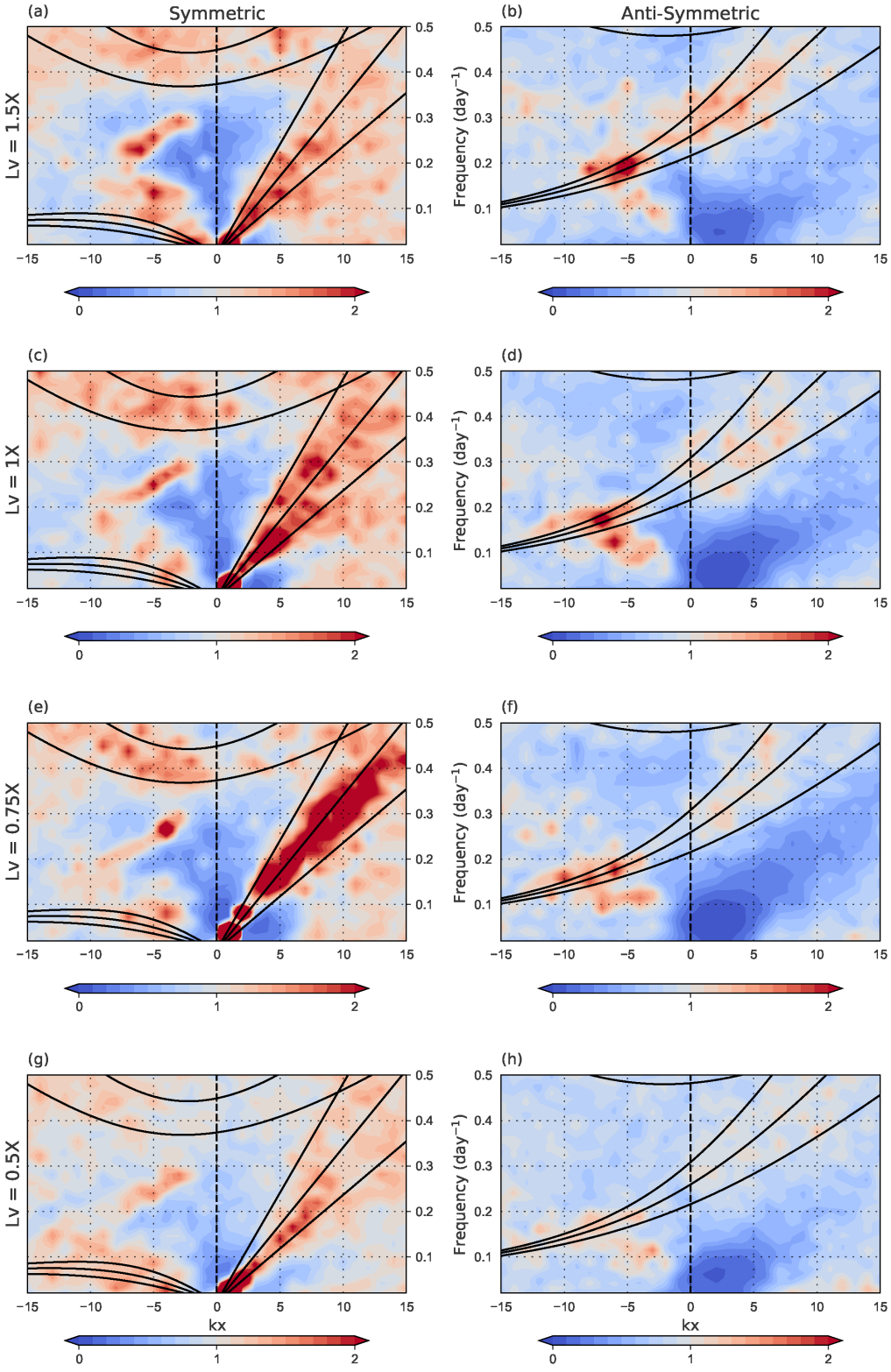

FIGURE 8
Frequency–wavenumber power spectra of zonal wind at 850 hPa for five different values of L_v. (a, c, e, g) show symmetric and (b, d, f, h) anti-symmetric components and the background spectra are removed. The power spectra are averaged over 15°N to 15°S latitudes. Superimposed are the dispersion curves (in black) for equivalent depths of 12, 25 and 50 m [Colour figure can be viewed at wileyonlinelibrary.com]

time-scales, approximately 7 to 15 days, due to the westward moving waves (Figure 10g). However, with weakened coupling, the westward component becomes comparable to the eastward modes, even at the lower frequencies (Figures 10 b, e, h). Although a sharp distinct peak is still visible for $L_v = 0.5X$ and $0.4X$, it broadens for L_v below $0.4X$. With even weaker coupling, especially for the cases with $L_v = 0.25X$ and below, rather than distinct peaks, the winds show more of a plateau that is spread around the period of a month (Figure 10c, f, i). The spectra are now completely dominated by the westward components at almost all the time-scales. This dominance of westward modes for low L_v runs implies off-equatorial convergence, thus driving "reversed" in Hadley cells (Figure 1).

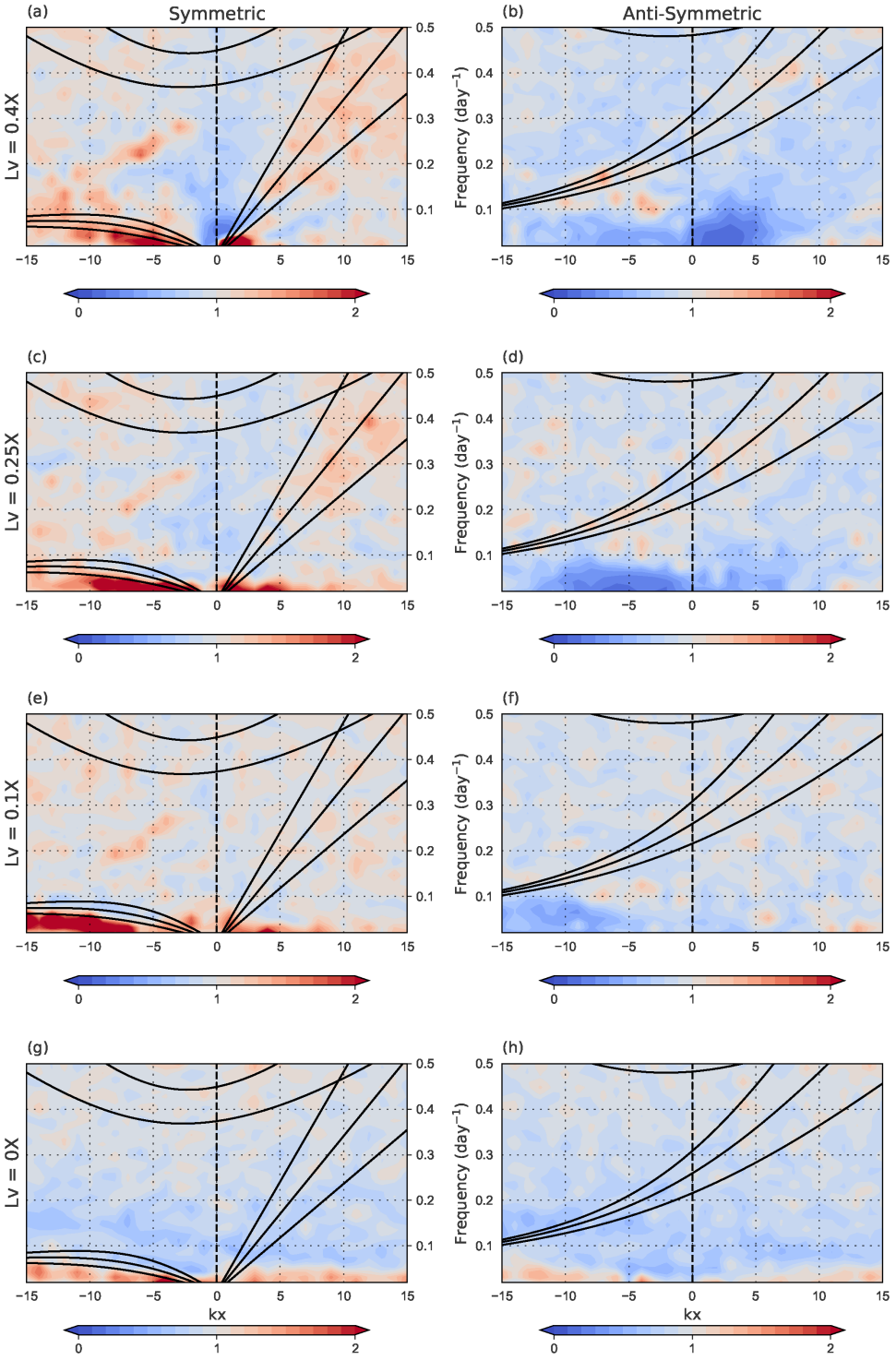

FIGURE 9 As Figure 8, but for smaller values of L_v [Colour figure can be viewed at wileyonlinelibrary.com]

Taken together, a broad picture that emerges in the Tropics is that of an overturning cell driven by wave-induced convergence, and progressively longer-period intraseasonal variability that aligns with familiar tropical dispersion curves and co-exists with smaller-scale (predominantly rotational) turbulence for stronger moist coupling.

With regard to transients at higher latitudes, a snapshot of the lower-level relative vorticity (850 hPa) for day 1,000 is shown in Figure 11. Much like prior observations in the f-plane (Held and Zhao, 2008) and global (Shi and Bretherton, 2014; Chavas and Reed, 2019) uniform SST simulations, intense cyclonic structures can be seen in the Extratropics for relatively strong coupling. Animations of the vorticity field suggest that these storm-like vortices are born in the Subtropics, sometimes merge to form larger structures and progress westward and towards the poles, due to β-drift (Shi and Bretherton, 2014). In fact, these storms are responsible for the poleward transport of

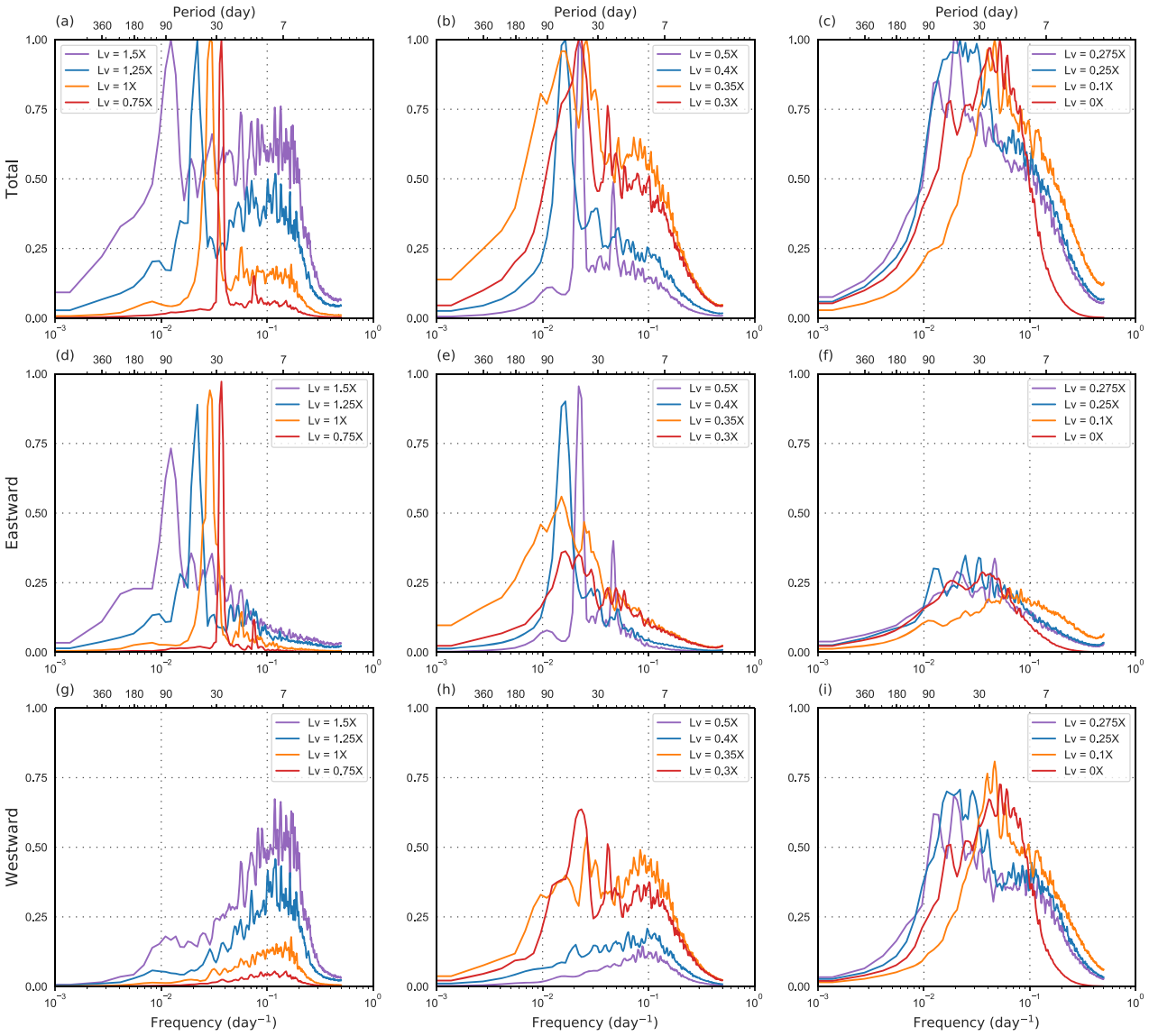

FIGURE 10 Variance-preserving normalized spectra and the corresponding east and west filtered components. The spectra are calculated for the zonal wind at 850 hPa and averaged over the latitudes 15°N to 15°S. [Colour figure can be viewed at wileyonlinelibrary.com]

both dry and latent energy as noted in Figure 5. The lifetime of these systems is approximately of the order of a month. The vertical profile of a typical storm for different L_v values is shown in Figure 12a, b. Here, the vorticity anomaly has a maximum in the lower troposphere and the system has a warm core with largest temperature anomalies in the upper troposphere. Thus, even though these storms are observed at higher latitudes, they are broadly similar to present-day tropical cyclones (Wang and Jiang, 2019) and some tropical lows (Kushwaha *et al.*, 2021). Indeed, for $L_v = 1X$, the largest temperature anomaly is at approximately 300 hPa and has a value of about 6 K, both aspects being comparable to present-day Category 1 tropical cyclones (Wang and Jiang, 2019). The fact that such cyclones are supported at higher latitudes in these simulations is likely tied to the vertical thermal structure of the atmosphere, especially its similarity with tropical regions (Figure 4). The magnitude of temperature anomalies and their spatial scale, and to a lesser extent the strength of the vorticity anomaly, decrease with lower latent heats, and in the dry simulation (Figures 11c, d and 12). Specifically, the storms smoothly transition from having a top-heavy strong temperature anomaly structure to a relatively constant (in height) weak and warm anomaly by $L_v = 0.5X$. A similar pattern emerged in simulations of cyclones with increasing surface dryness (Cronin and Chavas, 2019). This change in morphology is starkly captured in the probability density function (PDF) of the 850 hPa relative vorticity field as shown in Figure 12c. Quite clearly, for strong coupling, the PDF is fat-tailed

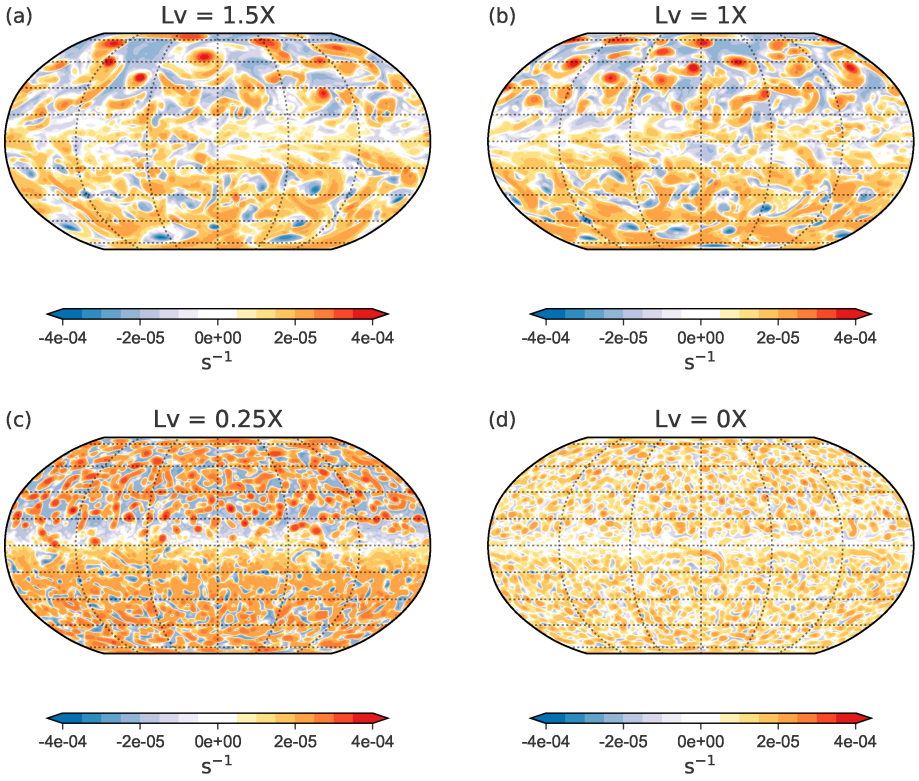

FIGURE 11 Snapshot of relative vorticity at 850 hPa on day 1,000 for four different values of L_v. The contour levels are logarithmic in nature with magnitude doubling between successive contours [Colour figure can be viewed at wileyonlinelibrary.com]

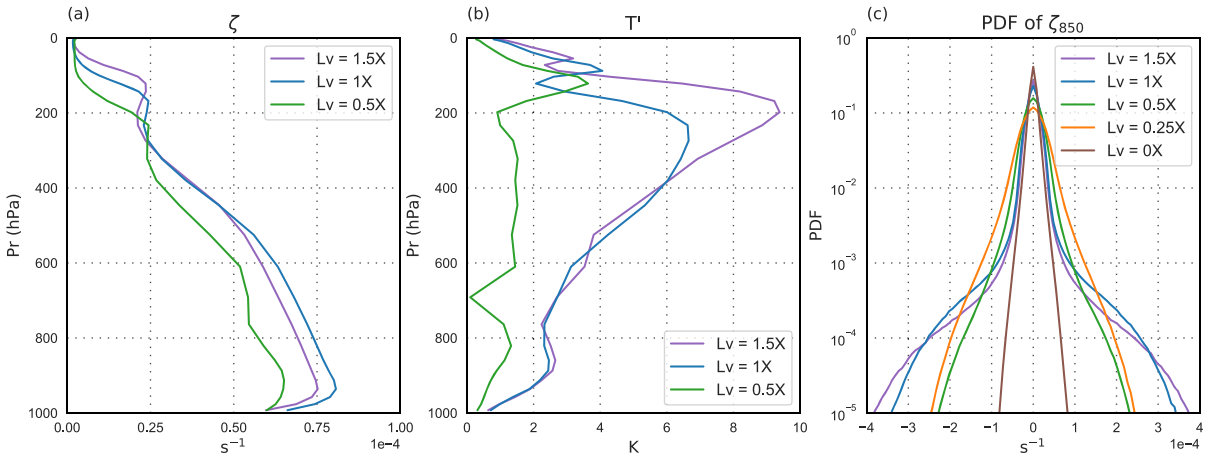

FIGURE 12 Vertical profiles of (a) relative vorticity and (b) temperature anomaly inside the cyclonic structure, computed by averaging over multiple cyclonic structures. Temperature anomaly is defined as the deviation from the global average at each vertical level. (c) shows the probability density function of relative vorticity field at 850 hPa. The same colour coding is used as in Figure 4 [Colour figure can be viewed at wileyonlinelibrary.com]

with a high propensity of extremes associated with intense cyclones, whereas for progressively smaller coupling the PDF tends to have exponential tails (seen as straight lines in the semi-log plot of Figure 12c).

4.1 | Nature of precipitation

Snapshots of the daily precipitation fields are shown in Figure 13. For stronger coupling (say for example, L_v = 1.5X) intense rainfall events (dark colours in Figure 13a) have a very different character in the Tropics and mid-latitudes. The former have a wave-like nature while the latter are clearly associated with vortices. As latent heat decreases, rainfall is more evenly distributed, with relatively higher variability near the Tropics and Subtropics. Further, with weaker coupling, the precipitation has a peak at the Subtropics (also seen in Figure 14a), corresponding to the ascending motion in the subtropical region (Figure 1). However, with stronger coupling the

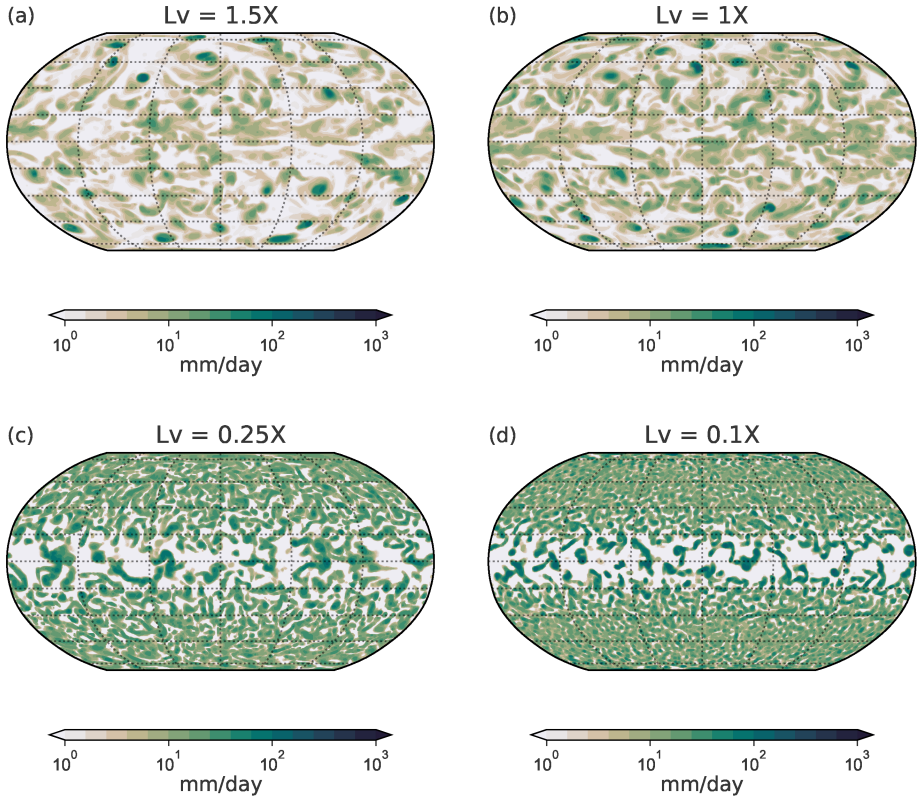

FIGURE 13 Snapshots of the daily precipitation at day 1,000 for four different values of L_v. Note that the colour scale is logarithmic [Colour figure can be viewed at wileyonlinelibrary.com]

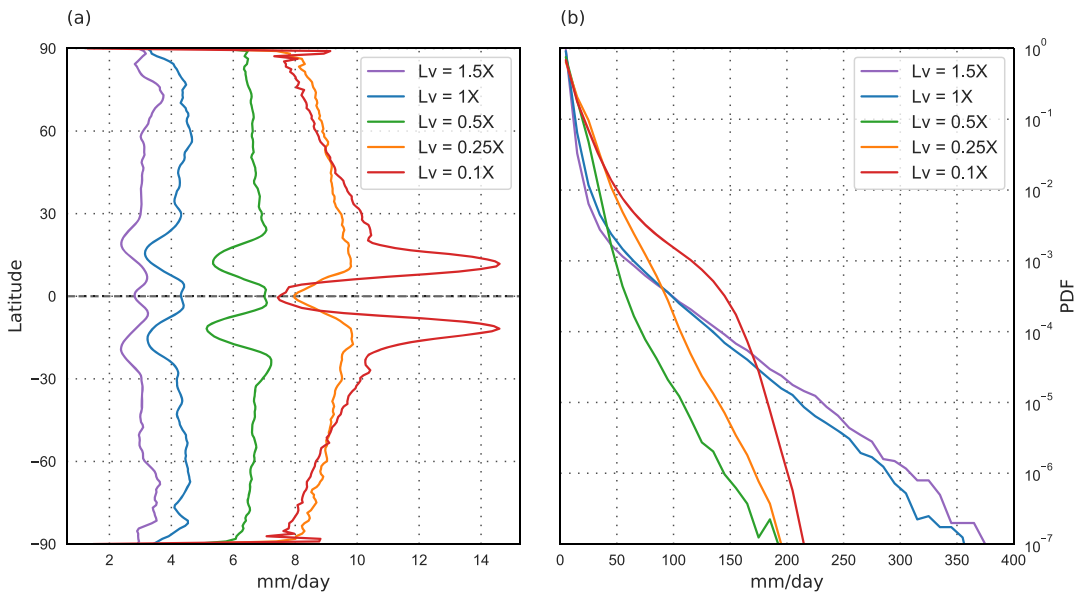

FIGURE 14 (a) Zonal mean precipitation and (b) probability density function of the daily mean precipitation, for different values of L_v. The same colour coding is used as in Figure 4 [Colour figure can be viewed at wileyonlinelibrary.com]

precipitation has an equatorial peak (at least locally), consistent with the ascending motion in the Tropics (Figure 1). Thus, the nature of the Hadley cell seen in Figure 1, especially its change in direction of overturning, is in line with the zonal mean precipitation. In fact, the near-equatorial region gets progressively devoid of strong rainfall events with decreasing L_v, which is consistent with the loss of Kelvin and MJO-like modes (Figures 8 and 9). Rossby waves survive for smaller L_v, and are likely responsible for the between gyre or meridionally aligned events in Figure 13c, d (Wheeler *et al.*, 2000; Suhas and Sukhatme, 2020). Given that there are no meridional gradients at the surface, the organization of moist convection in the Tropics by equatorial waves likely gives rise

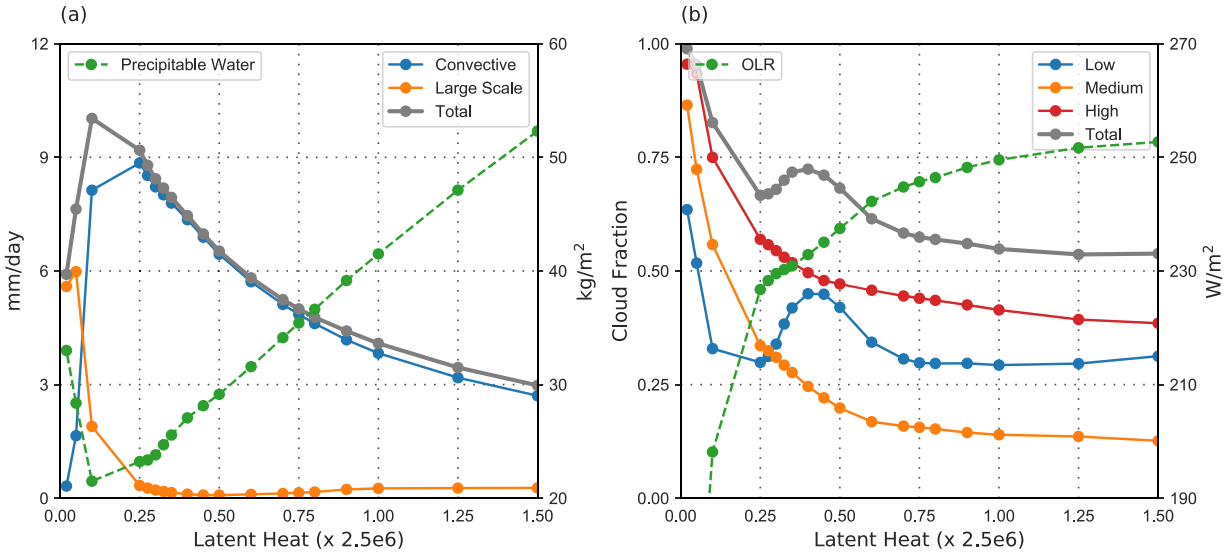

FIGURE 15 Globally averaged (a) precipitation and precipitable water and (b) cloud fraction and OLR, as a function of latent heat L_v [Colour figure can be viewed at wileyonlinelibrary.com]

to precipitation patterns, which in turn, via latent heating couple to result in large-scale ascent and the overturning flow (Horinouchi, 2012). The connection of tropical wave activity to the Hadley cell is also supported by the fact that the width of these tropical cells, while not an exact match, follows the same pattern as the equatorial deformation scale in Figure 7.

Interestingly, precipitation is actually higher for lower latent heat values at all latitudes, as is seen in Figure 14a. The distribution of these precipitation events (Figure 14b) shows that, while the larger latent heat cases have a higher chance of extreme rainfall (up to 400 mm·day^{-1}), the lower latent heat runs have a higher probability of comparatively moderate rainfall events (about 50–150 mm·day^{-1}). A similar picture emerges in Figure 15a, with the global mean precipitation increasing with decreasing latent heat. Note that precipitable water increases with moist coupling (Figure 15a), perhaps suggesting that, with decrease in precipitation, more precipitable water is stored in the atmosphere. Consistent with the behaviour of precipitation, cloud fraction also increases with decreasing L_v (Figure 15b). This increase is mainly due to changes in the medium and high cloud cover. We also see that outgoing LW radiation (OLR) saturates at high L_v (Figure 15b), possibly as a result of the increase in water vapour (Koll and Cronin, 2018). Overall, as OLR saturates and the SST is fixed, this results in tropospheric temperature profiles (Figure 4b, c) which imply an increase in stability for larger L_v in the middle and upper troposphere. In turn, this possibly affects middle and high clouds and accounts for the observed decrease in precipitation and cloud fraction (Bony *et al.*, 2016). Interestingly, recent explorations of moist and dry warm-core cyclones have also shown an increase in cloud fraction for relatively drier conditions (Cronin and Chavas, 2019).

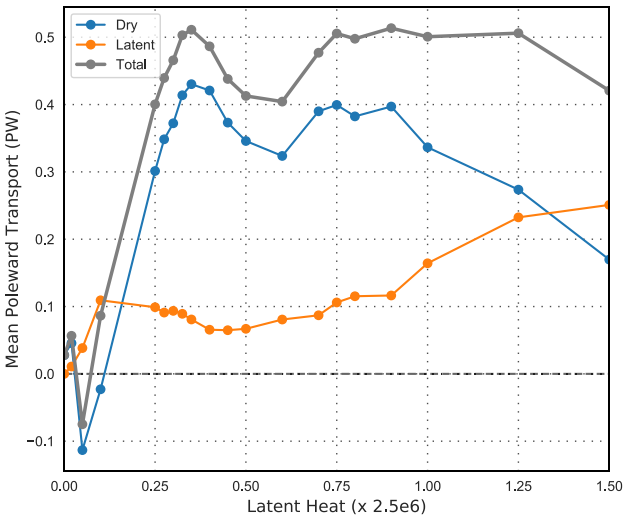

FIGURE 16 Global mean poleward transport of energy as a function of latent heat L_v. [Colour figure can be viewed at wileyonlinelibrary.com]

5 | CONCLUSION AND DISCUSSION

We have explored the various aspects of dynamically dry and moist atmospheric circulations using a 3D aquaplanet model with uniform lower boundary conditions. The degree or strength of moist coupling was controlled by systematically varying the latent heat of water vapour (L_v), and with $L_v \to 0$, water substance is essentially a passive

tracer from a dynamical point of view. This allows one not only to contrast the moist and dry dynamics, but also to look at the emergent dynamics in the intermediate moist coupling regimes. In all these experiments, even though the SST is fixed, the atmosphere is in energy balance.

Despite the absence of meridional thermal gradients, we observe a general circulation with Hadley and Ferrel cells. These cells are of comparable magnitude to those on present-day Earth. However, the nature of the Hadley cell is very different from an Earth-like scenario where the surface temperature gradient and midlatitude baroclinic waves play a prominent role in determining its direction, strength and terminus (Levine and Schneider, 2015); in fact, as suggested by Horinouchi (2012), tropical overturning is dictated by the organization of convergence via equatorial waves. For relatively strong moist coupling, Kelvin and MJO-like modes dominate, leading to equatorial convergence, thus driving a traditional overturning circulation. Whereas, for weaker moist coupling ($L_v \leq 0.25X$), Rossby waves dominate the tropical regions, convergence is off-equatorial and the mean circulation reverses with a poleward surface transport in the Tropics. The transition between these two regimes occurs at approximately $L_v = 0.3X$. Another rather abrupt change takes place in the limiting case of a dry atmosphere; here the height of the circulation dramatically reduces, suggesting the importance of moist processes in sustaining the deep convection. Further, tropical cells are thermally indirect and likely also influenced by eddy momentum fluxes. Easterlies form through most of the troposphere with a small region of super-rotation in the upper Tropics. The magnitude of super-rotation weakens and disappears as water vapour becomes passive. Eddy momentum flux convergence is responsible for driving the zonal mean flow in the Tropics. In fact, these fluxes are prominent in both the upper and lower troposphere, thus serving as an intermediate regime between the present-day Earth and high-obliquity planets with reverse meridional surface temperature gradients, where fluxes are largely confined to the upper and lower troposphere, respectively (Ait-Chaalal and Schneider, 2015; Kang *et al.*, 2019). While the direction of the tropical overturning remains consistent beyond $L_v = 0.3X$, another transition occurs in the upper-level winds at slightly stronger moist coupling. Specifically, the zonal flow in the midlatitudes is mostly westward, but westerlies emerge with a weakened moist coupling ($L_v < 0.5X$). This change in direction of the zonal wind is consistent with the sign of the upper tropospheric meridional temperature gradient in each of these runs, which changes from poleward to equatorward at $L_v = 0.5X$.

As expected, the zonal mean dry static energy flux is dominated by the upper-level circulation, while the latent heat flux mimics the direction of mean circulation at the surface. In the Tropics and subtropical Ferrel cell regions, MSE transport is determined by the difference of these two opposing components. In all the cases, MSE transport is equatorward in the Tropics and poleward in the midlatitudes, with a net poleward transport when averaged over all latitudes (Figure 16). In addition, transport in the Tropics and midlatitudes is largely due to the mean flow and eddy components, respectively, with transport in the subtropical Ferrel-cell regions resulting from both. It should be noted that the transport of energy in the Tropics and midlatitudes is quite different from present-day Earth (Pierrehumbert, 2002; Trenberth and Stepaniak, 2003) in that, in the Tropics, the latent flux is larger than the dry term and the net result is an equatorward transport of energy, and in the midlatitudes, both the latent and dry terms are important and directed poleward. Remarkably the magnitude of the hemispherically averaged MSE transport remains roughly invariant from $L_v = 1.5X$ to $0.25X$, and then falls drastically as water substance becomes almost passive. Much like the observations of Frierson *et al.* (2007), the nearly constant transport for $L_v > 0.8X$ is due to an increase of dry static energy transport that compensates the decreasing latent heat component with L_v. For $0.25X < L_v < 0.8X$, there is a transition from moist warm-core vortices dominating the transport at higher L_v to waves dominating the transport at lower L_v, and correspondingly the global poleward mean MSE flux varies a little more in this range than for larger L_v.

Transients in the Tropics and midlatitudes are also profoundly affected by the moisture interactions. Global kinetic energy spectra for the relatively strong coupling runs have some similarities to the Earth's atmosphere; specifically, the power spectrum is characterized by an approximate slope of -3 to -4 at large scales and is dominated by rotational modes. However, in contrast to the present-day Earth, there are no signs of a transition to a shallower slope at smaller scales. With weakening moist coupling, the deformation scale reduces with a corresponding shift in the peak of energy spectra towards the smaller scales and an overall flattening of spectra. In fact, in the passive run, the spectrum suggests a broad peak in variance at about the deformation scale. In the Tropics, for stronger coupling, most of the large-scale variability lies along familiar equatorial modes with Earth-like speeds and there is a systematic increase in the time period of these systems with progressively stronger coupling. In particular, as L_v goes from $0.75X$ to $1.5X$, the dominant peak of activity moves from about a month to 90 days. Further, intraseasonal modes, especially the eastward moving MJO-like structure and Kelvin waves, disappear as water substance becomes dynamically passive. The lack of a MJO-like mode for the passive case

suggests the vital and possibly essential role played by interactive moisture in its dynamics. In accord with the spatial energy spectrum, the passive case does not have much energy at large scales. Furthermore, the change in prominent intraseasonal waves with L_v, that is, Kelvin and MJO-like modes at large L_v and Rossby waves for smaller L_v, leads to on- and off-equatorial convergence and hence determines the direction of the tropical overturning flow. The midlatitudes are characterised by multiple tropical storm-like warm-core vortices, drifting poleward and westward over a time period of a month. The lack of baroclinic instability due to the absence of imposed meridional thermal gradients, and the conditionally unstable nature of the temperature profiles, possibly favour the existence of warm-core vortices similar to the Earth-like tropical cyclones even at higher latitudes. These vortices are associated with extreme rainfall events, and are responsible for a poleward MSE transport in midlatitudes. As with the "dry" simulations of tropical cyclones (Cronin and Chavas, 2019), when water substance becomes passive, the storm-like vortices become less intense, smaller in size and their temperature anomalies decrease. The change in their vorticity field is succinctly captured by the shift from a PDF with fat tails (large L_v) to one with a purely exponential form (small L_v). The change from present-day wave-like disturbances to warm-core vortices seems to have very strong implications for the zonal mean energy budget and mean temperature structure. While wave disturbances act to mix background gradients diffusively, the moist and warm vortices which move poleward due to a beta-drift carry MSE poleward regardless of the direction of the background MSE gradient. As a result, the vortex world has warmer poles and an up-gradient MSE flux, while the wave world has colder poles and down-gradient MSE fluxes.

Snapshots of intense precipitation suggest a change in morphology between tropical and midlatitude events; the former are wave-like while the latter are in the form of vortices. With decreasing L_v, the region near the Equator is progressively devoid of intense rainfall; this goes hand in hand with the loss of Kelvin and MJO-like modes. Interestingly, global mean precipitation increases with weaker moist coupling, with an opposing trend shown by the precipitable water. In essence, extreme rainfall events decrease, but there is more rainfall with weaker coupling of water substance. The decrease in rainfall and mid- to upper-level cloud fraction with increasing L_v appears to be tied to the mechanism proposed by Bony *et al.* (2016), involving increased static stability of the troposphere at middle and upper levels. More fundamentally, OLR saturates as L_v increases, hence with fixed SSTs the system responds with an increase in tropospheric temperature. This appears to be the cause of an increased static stability and results in lower amounts of total precipitation with strong coupling of water vapour.

We believe that the results from these simulations, much like the moist and dry scenarios studied by Frierson *et al.* (2006; 2007), will help in developing a more robust view of planetary atmospheric circulation regimes in the presence of a condensable substance. In particular, the flexibility of our approach could also be of use in probing the dynamics of planetary atmospheres with condensable substances that have latent heat significantly different from water vapour. From a general circulation point of view, these simulations show a very different way of obtaining tropical and extratropical regimes. Specifically, we have a Hadley cell with a well-defined terminus but, rather than demarcating the change to a baroclinic wave-dominated regime (Levine and Schneider, 2015), here the transition is to storm-like warm-core vortices. Indeed, the Hadley cell itself is driven by convergence due to the equatorial waves and their modulation of latent heating, rather than a surface temperature gradient. In fact, the width of the Hadley cell is seen to decrease with L_v, and this seems to be directly connected to the equatorial deformation scale. In fact, conditions on Earth with significantly weaker meridional surface temperature gradients (Brierley *et al.*, 2009) might be susceptible to overturning flows driven in this manner. Further, similar to emerging details on the possibility of warm-core cyclones in dry simulations (Mroweic *et al.*, 2011; Cronin and Chavas, 2019; Wang and Lin, 2020) and their implications for real-world cyclonic systems, the effects of varying moist coupling on transient activity could prove to be of use in a more basic understanding of the moist modes of tropical intraseasonal variability.

ACKNOWLEDGEMENTS

We would like to thank the Supercomputing Education and Research Centre (SERC) at IISc for computer facilitites where most of these simulations were carried out. This work was funded by a joint India–Israel grant, under the Indian University Grants Commission grant number F6-3/2018 and the Israeli Science Foundation grant number 2713/17.

AUTHOR CONTRIBUTIONS

D. L. Suhas: conceptualization; data curation; formal analysis; investigation; methodology; validation; visualization; writing – original draft; writing – review and editing. **Jai Sukhatme:** conceptualization; formal analysis; funding acquisition; investigation; methodology; project administration; resources; supervision; validation; writing – original draft; writing – review and

editing. **Nili Harnik:** conceptualization; formal analysis; funding acquisition; investigation; methodology; project administration; supervision; validation; writing – original draft; writing – review and editing.

ORCID

D. L. Suhas https://orcid.org/0000-0001-7453-867X

REFERENCES

Adames, A.F. and Kim, D. (2016) The MJO as a dispersive, convectively coupled moisture wave: theory and observations. *Journal of the Atmospheric Sciences*, 73(3), 913–941. https://doi.org/10.1175/JAS-D-15-0170.1.

Ait-Chaalal, F. and Schneider, T. (2015) Why eddy momentum fluxes are concentrated in the upper troposphere. *Journal of the Atmospheric Sciences*, 72(4), 1585–1604. https://doi.org/10.1175/JAS-D-14-0243.1.

Arnold, N.P. and Randall, D.A. (2015) Global-scale convective aggregation: implications for the Madden–Julian Oscillation. *Journal of Advances in Modeling Earth Systems*, 7(4), 1499–1518. https://doi.org/10.1002/2015MS000498.

Barsugli, J., Shin, S. and Sardeshmukh, P.D. (2005) Tropical climate regimes and global climate sensitivity in a simple setting. *Journal of the Atmospheric Sciences*, 62(4), 1226–1240. https://doi.org/10.1175/JAS3404.1.

Bartello, P. (1995) Geostrophic adjustment and inverse cascades in rotating stratified turbulence. *Journal of the Atmospheric Sciences*, 52(24), 4410–4428. https://doi.org/10.1175/1520-0469(1995)052<4410:GAAICI>2.0.CO;2.

Becker, T., Stevens, B. and Hohenegger, C. (2017) Imprint of the convective parameterization and sea-surface temperature on large-scale convective self-aggregation. *Journal of Advances in Modeling Earth Systems*, 9(2), 1488–1505.

Bony, S., Stevens, B., Coppin, D., Becker, T., Reed, K.A., Voigt, A. and Medeiros, B. (2016) Thermodynamic control of anvil cloud amount. *Proceedings of the National Academy of Sciences*, 113, 8927–8932. https://doi.org/10.1073/pnas.1601472113.

Bretherton, C.S. and Park, S. (2009) A new moist turbulence parameterization in the Community Atmosphere Model. *Journal of Climate*, 22(12), 3422–3448. https://doi.org/10.1175/2008JCLI2556.1.

Bretherton, C.S., Blossey, P.N. and Khairoutdinov, M. (2005) An energy-balance analysis of deep convective self-aggregation above uniform SST. *Journal of the Atmospheric Sciences*, 62(12), 4273–4292. https://doi.org/10.1175/JAS3614.1.

Brierley, C.M., Fedorov, A.V., Liu, Z., Herbert, T.D., Lawrence, K.T. and Lariviere, J.P. (2009) Greatly expanded tropical warm pool and weakened Hadley circulation in the early pliocene. *Science*, 323(5922), 1714–1718. https://doi.org/10.1126/science.1167625.

Bühler, O., Callies, J. and Ferrari, R. (2014) Wave-vortex decomposition of one-dimensional ship-track data. *Journal of Fluid Mechanics*, 756, 1007–1026. https://doi.org/10.1017/jfm.2014.488.

Chavas, D.R. and Reed, K.A. (2019) Dynamical aquaplanet experiments with uniform thermal forcing: system dynamics and implications for tropical cyclone genesis and size. *Journal of the Atmospheric Sciences*, 76(8), 2257–2274. https://doi.org/10.1175/JAS-D-19-0001.1.

Coppin, D. and Bony, S. (2015) Physical mechanisms controlling the initiation of convective self-aggregation in a general circulation model. *Journal of Advances in Modeling Earth Systems*, 7(4), 2060–2078.

Cronin, T.W. and Chavas, D.R. (2019) Dry and semidry tropical cyclones. *Journal of the Atmospheric Sciences*, 76, 2193–2212. https://doi.org/10.1175/JAS-D-18-0357.1.

Das, S., Sengupta, D., Chakraborty, A., Sukhatme, J. and Murtugudde, R. (2016) Low-frequency intraseasonal variability in a zonally symmetric aquaplanet model. *Meteorology and Atmospheric Physics*, 128(6), 697–713. https://doi.org/10.1007/s00703-016-0448-y.

Dima, I.M. and Wallace, J.M. (2003) On the seasonality of the Hadley cell. *Journal of the Atmospheric Sciences*, 60(12), 1522–1527. https://doi.org/10.1175/1520-0469(2003)060<1522:OTSOTH>2.0.CO;2.

Dima, I.M., Wallace, J.M. and Kraucunas, I. (2005) Tropical zonal momentum balance in the NCEP reanalyses. *Journal of the Atmospheric Sciences*, 62(7), 2499–2513. https://doi.org/10.1175/JAS3486.1.

Emanuel, K.A. (1995) On thermally direct circulations in moist atmospheres. *Journal of the Atmospheric Sciences*, 52(9), 1529–1534. https://doi.org/10.1175/1520-0469(1995)052<1529:OTDCIM>2.0.CO;2.

Fedorov, A.V., Brierley, C.M. and Emanuel, K.A. (2010) Tropical cyclones and permanent El Niño in the early Pliocene epoch. *Nature*, 463, 1066–1070. https://doi.org/10.1038/nature08831.

Fedorov, A.V., Muir, L., Boos, W.R. and Studholme, J. (2019) Tropical cyclogenesis in warm climates simulated by a cloud-system resolving model. *Climate Dynamics*, 52(1-2), 107–127. https://doi.org/10.1007/s00382-018-4134-2.

Frierson, D.M.W. (2007) Convectively coupled Kelvin waves in an idealized moist general circulation model. *Journal of the Atmospheric Sciences*, 64(6), 2076–2090. https://doi.org/10.1175/JAS3945.1.

Frierson, D.M.W., Held, I.M. and Zurita-Gotor, P. (2006) A gray-radiation aquaplanet moist GCM. Part I: static stability and eddy scale. *Journal of the Atmospheric Sciences*, 63(10), 2548–2566. https://doi.org/10.1175/JAS3753.1.

Frierson, D.M.W., Held, I.M. and Zurita-Gotor, P. (2007) A gray-radiation aquaplanet moist gcm. Part II: energy transports in altered climates. *Journal of the atmospheric sciences*, 64(5), 1680–1693. https://doi.org/10.1175/JAS3913.1.

Grabowski, W.W. (2003) MJO-like coherent structures: sensitivity simulations using the cloud-resolving convection parameterization (CRCP). *Journal of the Atmospheric Sciences*, 60(6), 847–864. https://doi.org/10.1175/1520-0469(2003)060<0847:MLCSSS>2.0.CO;2.

Grabowski, W.W. and Moncrieff, M.W. (2004) Moisture–convection feedback in the tropics. *Quarterly Journal of the Royal Meteorological Society*, 130, 3081–3104. https://doi.org/10.1256/qj.03.135.

Held, I.M. and Zhao, M. (2008) Horizontally homogeneous rotating radiative–convective equilibria at GCM resolution. *Journal of the Atmospheric Sciences*, 65(6), 2003–2013. https://doi.org/10.1175/2007JAS2604.1.

Holton, J.R. and Hakim, G. (2012) *An Introduction to Dynamic Meteorology* (5th edition). New York, NY: Academic Press.

Horinouchi, T. (2012) Moist Hadley circulation: possible role of wave–convection coupling in aquaplanet experiments. *Journal*

of the Atmospheric Sciences, 69(3), 891–907. https://doi.org/10.1175/JAS-D-11-0149.1.

Kang, W., Cai, M. and Tziperman, E. (2019) Tropical and extratropical general circulation with a meridional reversed temperature gradient as expected in a high obliquity planet. *Icarus*, 330, 142–154. https://doi.org/10.1016/j.icarus.2019.04.028.

Khairoutdinov, M. and Emanuel, K. (2013) Rotating radiative-convective equilibrium simulated by a cloud-resolving model. *Journal of Advances in Modeling Earth Systems*, 5(4), 816–825. https://doi.org/10.1002/2013MS000253.

Kirtman, B.P. and Schneider, E.K. (2000) A spontaneously generated tropical atmospheric general circulation. *Journal of the Atmospheric Sciences*, 57(13), 2080–2093. https://doi.org/10.1175/1520-0469(2000)057<2080:ASGTAG>2.0.CO;2.

Kitamura, Y. and Matsuda, Y. (2006) The k_H^{-3} and $k_H^{-5/3}$ energy spectra in stratified turbulence. *Geophysical Research Letters*, 33(5). https://doi.org/10.1029/2005GL024996.

Koll, D.D.B. and Cronin, T.W. (2018) Earth's outgoing longwave radiation linear due to H_2O greenhouse effect. *Proceedings of the National Academy of Sciences*, 115, 10293–10298. https://doi.org/10.1073/pnas.1809868115.

Kushwaha, P., Sukhatme, J. and Nanjundiah, R.S. (2021) A global tropical survey of mid-tropospheric cyclones. *Monthy Weather Review*, 149, 2737–2753. https://doi.org/10.1175/MWR-D-20-0222.1.

Lee, S. (1999) Why are the climatological zonal winds easterly in the equatorial upper troposphere?. *Journal of the Atmospheric Sciences*, 56(10), 1353–1363. https://doi.org/10.1175/1520-0469(1999)056<1353:WATCZW>2.0.CO;2.

Levine, X. and Schneider, T. (2015) Baroclinic eddies and the extent of the Hadley circulation: an idealized GCM study. *Journal of the Atmospheric Sciences*, 72, 2744–2761. https://doi.org/10.1175/JAS-D-14-0152.1.

Lindborg, E. (2015) A Helmholtz decomposition of structure functions and spectra calculated from aircraft data. *Journal of Fluid Mechanics*, 762. https://doi.org/10.1017/jfm.2014.685.

Lutsko, N.J. (2018) The response of an idealized atmosphere to localized tropical heating: superrotation and the breakdown of linear theory. *Journal of the Atmospheric Sciences*, 75(1), 3–20. https://doi.org/10.1175/JAS-D-17-0192.1.

Maher, P., Gerber, E.P., Medeiros, B., Merlis, T.M., Sherwood, S., Sheshadri, A., Sobel, A.H., Vallis, G.K., Voigt, A. and Zurita-Gotor, P. (2019) Model hierarchies for understanding atmospheric circulation. *Reviews of Geophysics*, 57(2), 250–280. https://doi.org/10.1029/2018RG000607.

Medeiros, B., Williamson, D.L. and Olson, J.G. (2016) Reference aquaplanet climate in the Community Atmosphere Model, version 5. *Journal of Advances in Modeling Earth Systems*, 8(1), 406–424. https://doi.org/10.1002/2015MS000593.

Merlis, T., Zhou, W., Held, I.M. and Zhao, M. (2016) Surface temperature dependence of tropical cyclone-permitting simulations in a spherical model with uniform thermal forcing. *Geophysical Research Letters*, 43(6), 2859–2865. https://doi.org/10.1002/2016GL067730.

Merlis, T.M. and Held, I.M. (2019) Aquaplanet simulations of tropical cyclones. *Current Climate Change Reports*, 5(3), 185–195. https://doi.org/10.1007/s40641-019-00133-y.

Mitchell, J.L. and Lora, J.M. (2016) The climate of Titan. *Annual Review of Earth and Planetary Sciences*, 44, 353–380. https://doi.org/10.1146/annurev-earth-060115-012428.

Mroweic, A.A., Garner, S.T. and Paulius, O. (2011) Axisymmetric hurricane in a dry atmosphere: theoretical framework and numerical experiments. *Journal of the Atmospheric Sciences*, 68, 1607–1619. https://doi.org/10.1175/2011JAS3639.1.

Muller, C.J. and Held, I.M. (2012) Detailed investigation of the self-aggregation of convection in cloud-resolving simulations. *Journal of the Atmospheric Sciences*, 69(8), 2551–2565. https://doi.org/10.1175/JAS-D-11-0257.1.

Muller, C.J. and Romps, D.M. (2018) Acceleration of tropical cyclogenesis by self-aggregation feedbacks. *Proceedings of the National Academy of Sciences*, 115(12), 2930–2935. https://doi.org/10.1073/pnas.1719967115.

Nastrom, G.D. and Gage, K. (1985) A climatology of atmospheric wavenumber spectra of wind and temperature observed by commercial aircraft. *Journal of the Atmospheric Sciences*, 42, 950–960. https://doi.org/10.1175/1520-0469(1985)042<0950:ACOAWS>2.0.CO;2.

O'Gorman, P.A. and Schneider, T. (2006) Stochastic models for the kinematics of moisture transport and condensation in homogeneous turbulent flows. *Journal of the Atmospheric Sciences*, 63(11), 2992–3005. https://doi.org/10.1175/JAS3794.1.

Oueslati, B. and Bellon, G. (2013) Tropical precipitation regimes and mechanisms of regime transitions: contrasting two aquaplanet general circulation models. *Climate Dynamics*, 40(9), 2345–2358.

Oueslati, B. and Bellon, G. (2015) The double ITCZ bias in CMIP5 models: interaction between SST, large-scale circulation and precipitation. *Climate Dynamics*, 44(3-4), 585–607.

Pierrehumbert, R.T. (2002) The hydrologic cycle in deep-time climate problems. *Nature*, 419, 191–198. https://doi.org/10.1038/nature01088.

Pierrehumbert, R.T. (2010) *Principles of Planetary Climate*. Cambridge, UK: Cambridge University Press.

Pierrehumbert, R.T., Brogniez, H. and Roca, R. (2007). On the relative humidity of the Earth's atmosphere. In T. Schneider and A. Sodel (Eds.), *The Global Circulation of the Atmosphere*, pp. 143–185. Princeton, NJ: Princeton University Press.

Ramírez Reyes, A. and Yang, D. (2021) Spontaneous cyclogenesis without radiative and surface-flux feedbacks. *Journal of the Atmospheric Sciences*. https://doi.org/10.1175/JAS-D-21-0098.1.

Raymond, D.J. and Fuchs, Z. (2009) Moisture modes and the Madden–Julian Oscillation. *Journal of Climate*, 22(11), 3031–3046. https://doi.org/10.1175/2008JCLI2739.1.

Read, P.L. and Lewis, S.R. (2004) *The Martian Climate Revisited*. Berlin: Springer.

Reed, K.A. and Chavas, D.R. (2015) Uniformly rotating global radiative-convective equilibrium in the Community Atmosphere Model, version 5. *Journal of Advances in Modeling Earth Systems*, 7, 1938–1955. https://doi.org/10.1002/2015MS000519.

Rocha, C.B., Chereskin, T.K. and Gille, S.T. (2016) Mesoscale to submesoscale wavenumber spectra in Drake Passage. *Journal of Physical Oceanography*, 46, 601–620. https://doi.org/10.1175/JPO-D-15-0087.1.

Schneider, T. and Bordoni, S. (2008) Eddy-mediated regime transitions in the seasonal cycle of a Hadley circulation and implications for monsoon dynamics. *Journal of the Atmospheric Sciences*, 65(3), 915–934. https://doi.org/10.1175/2007JAS2415.1.

Shi, X. and Bretherton, C.S. (2014) Large-scale character of an atmosphere in rotating radiative-convective equilibrium. *Journal of Advances in Modeling Earth Systems*, 6(3), 616–629. https://doi.org/10.1002/2014MS000342.

Shi, X., Kim, D., Adames, A.F. and Sukhatme, J. (2018) WISHE-moisture mode in an aquaplanet simulation. *Journal of Advances in Modeling Earth Systems*, 10(10), 2393–2407. https://doi.org/10.1029/2018MS001441.

Sobel, A. (2002) Water vapor as an active scalar in tropical atmospheric dynamics. *Chaos*, 12(2), 451–459. https://doi.org/10.1063/1.1480795.

Sobel, A. and Maloney, E. (2013) Moisture modes and the eastward propagation of the MJO. *Journal of the Atmospheric Sciences*, 70(1), 187–192. https://doi.org/10.1175/JAS-D-12-0189.1.

Suhas, D.L. and Sukhatme, J. (2020) Moist shallow-water response to tropical forcing: initial value problems. *Quarterly Journal of the Royal Meteorological Society*, 146, 3695–3714. https://doi.org/10.1002/qj.3867.

Sukhatme, J. and Smith, L.M. (2008) Vortical and wave modes in 3D rotating stratified flows: random large-scale forcing. *Geophysical and Astrophysical Fluid Dynamics*, 102(5), 437–455. https://doi.org/10.1080/03091920801915318.

Sukhatme, J. and Young, W.R. (2011) The advection–condensation model and water-vapour probability density functions. *Quarterly Journal of the Royal Meteorological Society*, 137, 1561–1572. https://doi.org/10.1002/qj.869.

Sukhatme, J., Chaudhuri, D., MacKinnon, J., Shivaprasad, S. and Sengupta, D. (2020) Near-surface ocean kinetic energy spectra and small-scale intermittency from ship-based ADCP data in the Bay of Bengal. *Journal of Physical Oceanography*, 50, 2037–2052. https://doi.org/10.1175/JPO-D-20-0065.1.

Sumi, A. (1992) Pattern formation of convective activity over the aqua-planet with globally uniform sea surface temperature (SST). *Journal of the Meteorological Society of Japan. Ser. II*, 70(5), 855–876. https://doi.org/10.2151/jmsj1965.70.5_855.

Toniazzo, T., Bentsen, M., Craig, C., Eaton, B.E., Edwards, J., Goldhaber, S., Jablonowski, C. and Lauritzen, P.H. (2020) Enforcing conservation of axial angular momentum in the atmospheric general circulation model CAM6. *Geoscientific Model Development*, 13, 685–705. https://doi.org/10.5194/gmd-13-685-2020.

Trenberth, K.E. and Stepaniak, D.P. (2003) Covariability of components of poleward atmospheric energy transports on seasonal and interannual timescales. *Journal of Climate*, 16, 3691–3705. https://doi.org/10.1175/1520-0442(2003)016<3691:COCOPA>2.0.CO;2.

Vallgren, A., Deusebio, E. and Lindborg, E. (2011) Possible explanation of the atmospheric kinetic and potential energy spectra. *Physical Review Letters*, 107(26). https://doi.org/10.1103/PhysRevLett.107.268501.

Walker, C.C. and Schneider, T. (2005) Response of idealized Hadley circulations to seasonally varying heating. *Geophysical Research Letters*, 32(6). https://doi.org/10.1029/2004GL022304.

Walker, C.C. and Schneider, T. (2006) Eddy influences on Hadley circulations: simulations with an idealized GCM. *Journal of the Atmospheric Sciences*, 63(12), 3333–3350. https://doi.org/10.1175/JAS3821.1.

Wang, D. and Lin, Y. (2020) Size and structure of dry and moist reversible tropical cyclones. *Journal of the Atmospheric Sciences*, 77, 2091–2114. https://doi.org/10.1175/JAS-D-19-0229.1.

Wang, X. and Jiang, H. (2019) A 13-year global climatology of tropical cyclone warm-core structures from AIRS data. *Monthly Weather Review*, 147(3), 773–790. https://doi.org/10.1175/MWR-D-18-0276.1.

Wheeler, M. and Kiladis, G.N. (1999) Convectively coupled equatorial waves: analysis of clouds and temperature in the wavenumber–frequency domain. *Journal of the Atmospheric Sciences*, 56(3), 374–399. https://doi.org/10.1175/1520-0469(1999)056<0374:CCEWAO>2.0.CO;2.

Wheeler, M., Kiladis, G.N. and Webster, P.J. (2000) Large-scale dynamical fields associated with convectively coupled equatorial waves. *Journal of the Atmospheric Sciences*, 57(5), 613–640. https://doi.org/10.1175/1520-0469(2000)057<0613:LSDFAW>2.0.CO;2.

Williamson, D.L., Blackburn, M., Nakajima, K., Ohfuchi, W., Takahashi, Y.O., Hayashi, Y.Y., Nakamura, H., Ishiwatari, M., Mcgregor, J.L., Borth, H., Wirth, V., Frank, H., Bechtold, P., Wedi, N.P., Tomita, H., Satoh, M., Zhao, M., Held, I.M., Suarez, M.J., Lee, M.I., Watanabe, M., Kimoto, M., Liu, Y., Wang, Z., Molod, A., Rajendran, K., Kitoh, A. and Stratton, R.A. (2013) The aqua-planet experiment (APE): response to changed meridional SST profile. *Journal of the Meteorological Society of Japan. Series II*, 91, 57–89.

Wing, A.A. and Emanuel, K.A. (2014) Physical mechanisms controlling self-aggregation of convection in idealized numerical modeling simulations. *Journal of Advances in Modeling Earth Systems*, 6(1), 59–74. https://doi.org/10.1002/2013MS000269.

Wing, A.A., Emanuel, K., Holloway, C.E. and Muller, C. (2017). Convective self-aggregation in numerical simulations: a review. In R. Pincus, D. Winker, S. Bony, and B. Stevens (Eds.), *Shallow Clouds, Water Vapor, Circulation, and Climate Sensitivity*, pp. 1–25. Berlin: Springer, DOI 10.1007/s10712-017-9408-4, (to appear in print).

Wing, A.A., Stauffer, C.L., Becker, T., Reed, K.A., Ahn, M.S., Arnold, N.P., Bony, S., Branson, M., Bryan, G.H., Chaboureau, J.P., De Roode, S.R., Gayatri, K., Hohenegger, C., Hu, I.K., Jansson, F., Jones, T.R., Khairoutdinov, M., Kim, D., Martin, Z.K., Matsugishi, S., Medeiros, B., Miura, H., Moon, Y., M˝ uller, S.K., Ohno, T., Popp, M., Prabhakaran, T., Randall, D., Rios-Berrios, R., Rochetin, N., Roehrig, R., Romps, D.M., Ruppert Jr, J.H., Satoh, M., Silvers, L.G., Singh, M.S., Stevens, B., Tomassini, L., van Heerwaarden, C.C., Wang, S. and Zhao, M. (2020) Clouds and convective self-aggregation in a multimodel ensemble of radiative-convective equilibrium simulations. *Journal of Advances in Modeling Earth Systems*, 12(9). https://doi.org/10.1029/2020MS002138.

Zhang, G.J. and McFarlane, N.A. (1995) Sensitivity of climate simulations to the parameterization of cumulus convection in the Canadian Climate Centre general circulation model. *Atmosphere–Ocean*, 33, 407âĂŞ446.

Zhou, W., Held, I.M. and Garner, S.T. (2014) Parameter study of tropical cyclones in rotating radiative–convective equilibrium with column physics and resolution of a 25-km GCM. *Journal of the Atmospheric Sciences*, 71(3), 1058–1069. https://doi.org/10.1175/JAS-D-13-0190.1.

How to cite this article: Suhas, D.L., Sukhatme, J. & Harnik, N. (2022) Dry and moist atmospheric circulation with uniform sea-surface temperature. *Quarterly Journal of the Royal Meteorological Society*, 148(742), 35–56. Available from: https://doi.org/10.1002/qj.4191